Study on the Migrating Speed of Free Alternate Bars

Michihide Ishihara[1], **Hiroyasu Yasuda**[2]

[1]Graduate School of Science and Technology, Niigata University, Niigata, Japan
[2]Research Institute for Natural Hazards & Disaster Recovery Niigata University, Niigata, Japan

Key Points:

- The spatial distribution of the migrating speed of alternate bars that occur in rivers was determined.
- A hyperbolic partial differential equation for the bed level and a migrating speed formula were derived.
- The main dominant physical quantity of the migrating speed of alternate bars is the energy slope.

Corresponding author: Hiroyasu Yasuda, hiro@gs.niigata-u.ac.jp

Abstract

In this study, flume experiments were conducted under conditions where alternate bars occur, develop, and migrate, to understand the existence and scale of the spatial distribution of the migrating speed of alternate bars and their dominant physical quantities. In the flume experiment, the bed level and water level during the development of alternate bars were measured with high frequency and high spatial resolution. By comparing the geometric variation of the bed shape, the results showed that the migrating speed of the alternate bars is spatially distributed and changes with time. Next, to quantify the spatial distribution of the migrating speed of the alternate bars, a hyperbolic partial differential equation for the bed level and an calculating equation the migrating speed based on the advection term of the same equation were derived. Subsequently, the derived equation was shown to be applicable by comparing it with the measurements obtained in the flume experiments described above. The migrating speed of the alternate bars was calculated using above formulas, and it was found to have a spatial distribution that changed with the development of the alternate bars over time. The mathematical structure of the equation showed that the three dominant physical quantities of the migrating speed are the particle size, Shields number, and energy slope. In addition, our method is generally applicable to actual rivers, where the scale and hydraulic conditions are different from those in the flume experiments.

Plain Language Summary

Periodic river bed undulations, called alternate bars are spontaneously formed in rivers, which are located at sites from the alluvial fan to the natural embankment. The physical properties of these alternate bars are known to shift phases in a similar manner to water surface waves during floods. However, there is still a lack of understanding of the migrating speed of alternate bars. we first conducted a flume experiment under the condition that alternate bars can occur and develop. We measured the hydraulic quantity and bed shape using a high spatial resolution. Next, we quantified the migrating speed of the alternate bars using the measured values and the authors's model. This study determined that the migrating speed of the alternate bars has a spatial distribution, and it changes with time. Furthermore, the authors applied authors's model to a actual river during a flood event, and showed that it can provide good estimates of the migrating speed of alternate bars. This study will contribute to the systematic maintenance of river channels where the development and migration of bars are significant.

1 Introduction

Periodic forms can spontaneously occur along the surface of a river channel bed. These forms are called riverbed waves because of their geometrical shapes and physical properties. Riverbed waves can be classified as small-scale, mesoscale, and large-scale, depending on the spatial scales, which include the wavelength and wave height (Seminara, 2010). Small-scale riverbed waves have wavelengths on the scale of the water depth, whereas mesoscale riverbed waves have wavelengths on the river width scale and wave heights on the water depth scale. Large-scale riverbed waves have larger scales. The target of this study was the alternate bars that correspond to mesoscale riverbed waves. Alternate bars are riverbed waves that are spontaneously formed in rivers and are located at sites from the alluvial fan to the natural embankment. When observing alternate bars from the sky using aerial photographs (Fig. 1(a)), the tip part is diagonally connected to the left and right riverbanks; a deep-water pool is located downstream of this tip. Alternate bars can be broadly classified into two categories: 1) free bars, which occur naturally in straight channels

owing to the instability of the bottom surface, and 2) forced bars, which occur because of forcing derived from the channel's planar shape and boundary conditions(Seminara, 2010). In this study, among the above categories, free alternate bars are targeted. Because of the physical properties of these alternate bars, their phases are changed in a similar manner to water surface waves during floods of a magnitude that causes active sediment transport (Fig. 1(a),(b)). In the following sections, we detail the previous studies on free alternate bars.

Over the years, numerous studies have been conducted on alternate bars. One of the initial studies consisted of flume experiments that were performed by Kinoshita (Kinoshita, 1961). Kinoshita conducted long-term flume experiments to understand the dynamics of alternate bars that can produce meandering streams. He reported that 1) alternate bars have a globally uniform migrating speed and wavelength, 2) alternate bars in the early stages of development have short wavelengths and fast migrating speeds, and 3) the migrating speed becomes slower with the growth of wavelengths. These results have been confirmed in subsequent studies(Hiroshi, 1983; Yuichiro & Yoshio, 1985; Nobuhisa et al., 1999). In addition to the aforementioned conclusions, a formula was proposed to calculate the migrating speed of alternate bars based on experimental results, with the Froude number and shear velocity as the dominant physical quantities. However, the validity of this formula was not demonstrated in the same study.

In addition to studies using flume experiments, several studies have applied mathematical analyses to understand the mechanism of development of alternate bars. The first mathematical study on alternate bars was conducted by Callander (Callander, 1969), who extended the instability analysis proposed by Kennedy (Kennedy, 1963) for small-scale bed waves to a two-dimensional plane problem, and theoretically discussed the physical quantities that govern the generation of mesoscale riverbed waves. This study was the starting point for research aimed at predicting the conditions under which alternate bars occur and the wavelength and wave height of the alternate bars after development(Kuroki & Kishi, 1984; Colombini et al., 1987; Colombini & Tubino, 1991; Tubino, 1991; Schielen et al., 1993; Norihiro & Adichai, 2002; Bertagni & Camporeale, 2018). In these instability analyses, an equation for calculating the migrating speed of small bed perturbation was derived during analysis. Using the instability analysis, the migrating speed for each wave number was calculated. Kuroki(Kuroki & Kishi, 1984) et al. compared the calculated and measured values of the migrating speed and reported that the calculated value reproduced the measured value well. The calculated value is the migrating speed at the wavenumber of the maximum amplification rate, and the measured value is calculated from the time variation of the position of the tip of the bar. However, because the migrating speed obtained from the analysis corresponds to the wave number, its spatial distribution has neither been calculated nor determined from measurements.

With the emergence of instability analysis, numerical analyses of riverbed fluctuations during the occurrence and development of alternate bars began. Shimizu et al. (Shimizu & Itakura, 1989) reported for the first time that numerical analysis can satisfactorily reproduce each process of the occurrence and development of alternate bars. Recently, Federici et al. (Federici & Seminara, 2003) reported the propagation direction of small-bed perturbation by performing instability and numerical analyses.

Recent studies using flume experiments (Lanzoni, 2000a, 2000b; Miwa et al., 2007; Crosato et al., 2011, 2012; Venditti et al., 2012; Podolak & Wilcock, 2013) have investigated the effects of external factors, such as the amount of sediment supply and flow discharge, on the dynamics of alternate bars. Crosato et al. (Crosato et al., 2011, 2012) reported that alternate bars eventually shift from being migrating bars to steady bars; they performed flume experiments and a numerical analysis to verify this. Next, Venditti et al. (Venditti et al., 2012) reported that when sedi-

ment supply was interrupted after alternate bars occurred, the bed slope and Shields number decreased, and the bars disappeared accordingly. Podolak et al. (Podolak & Wilcock, 2013) studied the response of alternate bars to sediment supply by increasing the sediment supply during the occurrence and development of alternate bars. A non-migrating bar changed to a migrating bar with an increase in the bed slope and Shields number because of the increase in the sediment supply. This result from Podolak et al. was followed up in a subsequent study (Nelson & Morgan, 2018).

Several studies have also been conducted on real rivers (Eekhout et al., 2013; Adami et al., 2016). Eekhout et al.(Eekhout et al., 2013) investigated the dynamics of alternate bars in rivers for nearly three years and reported that the migrating speed decreased as the wavelength and wave height of alternate bars increased and the bed slope decreased. In addition, Adami et al.(Adami et al., 2016) studied the behavior of alternate bars in the Alps and Rhine River over several decades. They established the relationship between the flow discharge and migrating speed of bars and confirmed that bars move less when the flow rate is very high and move significantly when the flow discharge is in the middle scale of the flow discharge.

The geometry and physical properties of alternate bars have been investigated. Through previous studies, predicting the occurrence and geometry of alternate bars has become possible to some extent. In contrast, an understanding of the nature of the migrating speed of alternate bars is still lacking. In this study, considering the physics of alternate bars, which has not yet been fully demonstrated, we focused on the migrating speed and conducted the following experiments to clarify the dominant physical quantities, and the existence and scale of their spatial distribution and migrating speed. In Section 2, we describe the outline of the flume experiment using stream tomography (ST), which can simultaneously measure the geometric shapes of the water and bed surfaces with a high spatial resolution, and the measurement results. In Section 3, we assume that the alternate bars can be regarded as a wave phenomenon, and we derive a hyperbolic partial differential equation (HPDE) for the bed level. In this study, the advection velocity given to the advection term of the HPDE was used to calculate the migrating speed of the alternate bars. In Section 4, the validity of the calculation formula derived in Section 3 is verified based on the characteristics of the HPDE and the measured values of the bed level obtained in Section 2. In Section 5, the spatial distribution of the migrating speed of the alternate bars is quantified using the formula to calculate the migrating speed. In Section 6, the applicability of the above formula to real rivers is discussed. Section 7 describes the results obtained in Section 5, and Section 8 summarizes the research results.

2 Quantification of the Propagation Phenomenon in Alternate Bars Based on the Flume Experiment

2.1 Experimental Setup

Figure 2 shows a plan view of the experiment flume. The experimental channel consisted of a flume channel with a straight rectangular cross section. The flume had a length of 12.0 m, width of 0.45 m, and depth of 0.15 m. Fixed weirs with the same width as the flume were located 2.7 m from the upstream and downstream ends of the flume. Over the section 2.7–9.3 m from the upstream end that was sandwiched by these weirs, the initial bed of the channel for the experiment was a set flat bed. The bed was fabricated from a non-cohesive material with a mean diameter of 0.76 mm and the bed thickness was 5.0 cm.

For water supply to the channel, circulation-type pumping from a water tank at the downstream end to a water tank at the upstream end was adopted; water was

steadily supplied. The accuracy of the water discharge was confirmed using an electromagnetic flowmeter.

2.2 Experimental Condition

The purpose of this study is to understand the dominant physical quantities of the migrating speed of the alternate bars and the existence and scale of their spatial distribution. In the following experiment, we set up the hydraulic conditions under which alternate bars are expected to develop and migrate. It has been theoretically shown that the occurrence of alternate bars can be estimated using the river width–depth ratio (Callander, 1969; Kuroki & Kishi, 1984). Kuroki and Kishi(Kuroki & Kishi, 1984) showed that the type of bar that occurs can be classified based on $BI_0^{0.2}/h_0$. In this study, we set two conditions that correspond to the area of occurrence of alternate bars, as shown in Table. 1.

Table 1. Experimental condition.

Case	Flow discharge [L/s]	width [m]	slope	h_0 [m]	$BI_0^{0.2}/h_0$	β	τ_*
1	2.0	0.45	1/160	0.014	11.4	31.45	0.0713
2	2.6	0.45	1/200	0.018	8.7	25.13	0.0714

In Section 3, the HPDE for the bed level and the equation for calculating the advection velocity given to the advection term of the same equation are derived. Using these equations, we attempted to understand the existence and scale of the spatial distribution of the migrating speed of the alternate bars and the dominant physical quantity of the migrating speed.

The validity of the formula was verified by comparing the calculated values of the migrating speed of the instability analysis and the calculated values of the migrating speed derived in this study. Therefore, based on the characteristics of instability analysis, the conditions were set such that the particle size and Shields number were fixed, and the river width–depth ratio became a variable. The same experiment was conducted twice for each condition to confirm the reproducibility of the results.

These experimental conditions exceed the critical Shields number of 0.034 obtained from Iwagaki's equation (Yuichi, 1956). The sediment supply condition at the upstream end was set to no supply. The no-supply condition was chosen because preliminary experiments comparing the effects of the presence and absence of sediment supply on the spatial distribution of the migrating speed of alternate bars and its temporal variation showed that the spatial distribution of the migrating speed was more likely to expand in the no-supply condition.

Water flow was carried out for 2 h during this experiment with the aforementioned conditions. At this time, alternate bars developed, and their propagation and shape change became slow.

2.3 Measurement Method for the Bed Surface and Water Surface

In this study, we used ST, which was developed by Hoshino et al.(Hoshino et al., 2018), to measure the bed and water levels in a plane while the water was flowing. For details on the principles of the ST measurement, refer to Appendix A. In this study, the aforementioned measurements were performed with a spatial resolu-

tion of 2 cm^2 for every minute. The water depth was calculated from the difference between the water level and bed level. Because the ST measurements were missing near the side walls, the data of 0.38-m width excluding the side walls were used.

2.4 Measurement Results

In this section, we describe the migration phenomena of alternate bars based on high-resolution spatial measurements by the ST, using a plan view of the basal level of Fig. 3 and a longitudinal section of Fig. 4. The same figures show the measurement results of Condition 2, where typical alternate bars were formed. The results of the other condition differed from those of Condition 2 only in terms of the wavelength and wave height, but no essential difference was observed. For the results of the other condition, please refer to the database (https://doi.org/10.4121/16788778.v1).

Figure 3 shows the plan view of the deviation of the bed level by ST. The origin of the vertical coordinates of the ST is the flume bottom. Therefore, the water level and bed level represent the height from the bed of the flume. In this study, as mentioned earlier, ST measurements were taken at 1-min intervals for 2 h, but the results at 10-min intervals are described to facilitate the recognition of distinct changes in the set hydraulic conditions. Herein, the initial bed surface was created such that it was as flat as possible. However, obtaining a perfectly flat bed was difficult because of the accuracy limit of the bed surface that shapes the setup. Although the initial slope of the bed may affect the timing and development of alternate bars, the alternate bars that occurred and developed were similar to the trends observed in previous studies (Kinoshita, 1958; Federici & Seminara, 2003; Crosato et al., 2011; Venditti et al., 2012; Podolak & Wilcock, 2013). Given the purpose of this study, the initial slope of the river bed was not considered to be a concern.

First, it can be observed that the bottom shape did not change much from the initial flat bed in Fig. 3 from (a) to (d). Second, the bed topography in which deposition and scouring are alternately repeated in the downstream direction, that is, 2.0 m, 3.0 m, and 5.0 m from the upstream end, can be observed; thus, it can be confirmed that alternate bars occurred (Fig. 3(e)). In this study, we defined (e) 40 min, in which the geometric features of the alternate bars were confirmed from the measured result by the ST, as the occurrence time of the alternate bars. The alternate bars develop undulations with time, becoming more sedimented in the sedimented areas and more scoured in the scoured areas, which indicates that the entire bar is gradually migrating downstream. A series of observations from (g) 60 min to (m) 120 min of water flow shows that bars are migrating at a constant speed.

Next, Figure 4 shows the longitudinal distribution of the deviation in the bed level on the green dotted line in Fig. 3. Figure 4 shows (a) the initial stage of the experiment, (b) the occurrence of alternate bars, (c) the intermediate stage of the experiment, and (d) the final stage of the experiment. Figure 4 shows three results, where each one is 10 min apart. First, the deviation of the bed level was confirmed to maintain a nearly flat bed from 1 min to 20 min (Fig. 4(a)). After (b) 60 min, three bed undulations developed 2.5 m, 4.5 m, and 5.5 m from the upstream end. The amplitudes of the bed undulations developed, and they migrated in the downstream direction. This undulation migrated downstream with amplification of wave height from (b) 60 to 120 min of water flow. The above results indicate that the waviness of the alternate bars is being measured. In Fig. 4(d), a decrease in the bed level was observed in the upstream section because the experimental conditions were set to no sediment supply.

The linear wave theory indicates that the phase propagates without deforming the waveform if a wave propagates with a spatial and temporal constant migrating speed. Conversely, in nonlinear wave theory, in which the migrating speed has

a spatial distribution and temporal changes, the wave propagates with deformation of the waveform. From the viewpoint of the aforementioned wave theories, the migrating speed of the bars after the occurrence of alternate bars in (b) has a spatial distribution and is estimated to change with time, and it has the characteristics of a nonlinear wave.

3 Derivation of the Calculation Formula for the Migrating Speed of Alternate Bars

As shown in the previous section, the measurement results of this study show the nature of the wave in the process of the occurrence and development of alternate bars. These findings are similar to what has been reported in the literature (Kinoshita, 1958; Federici & Seminara, 2003; Crosato et al., 2011; Venditti et al., 2012; Podolak & Wilcock, 2013). In other words, there is scope for quantifying the spatial distribution of the migrating speed by an indirect method using a mathematical model such as the HPDE(Fujita Y., 1985), which is suitable for describing the wave phenomena. The formula for calculating the migrating speed is also derived from stability analysis (Callander, 1969; Kuroki & Kishi, 1984). However, because the formula calculates the migrating speed for each wave number, the spatial distribution of the migrating speed cannot be quantified. Another possible method is to set up feature points at the front edge of an alternate bar and to calculate the migrating speed based on the trajectory. However, both methods fail to obtain a continuous spatial distribution of the migrating speed. In addition, it is not possible to calculate the migrating speed using numerical analysis of the occurrence and development of bars. Therefore, in this study, we derived a hyperbolic partial differential equation for the bed level and quantified the spatial distribution of the migrating speed of alternate bars using the advection velocity, which is the coefficient of the advection term of the HPDE.

This section describes the derivation process of the HPDE for bed level z. In addition, four different formulas were obtained depending on the physical assumptions. This includes whether the dimension is one-dimensional or two-dimensional, and whether the flow is stationary or unsteady. First, regarding the stationarity of flow, as we confirmed that the non-stationary state in the phenomenon targeted by this study is very small from the verification results described in Appendix B, we decided to consider only the stationary state. In terms of dimensions, the geometric shape of the alternate bars and the flow each have two-dimensional plane characteristics. Therefore, we aimed to derive a two-dimensional stationary equation.

The derivation of the HPDE for the bed level can be used for the continuous equation of the sediment, sediment functions, and the equation of the water surface profile. For the derivation, the Exner equation was used as the continuous equation of the sediment, and the Meyer–Peter and Müller (MPM) formula were used as the sediment function and two-dimensional equation of the water surface profile, respectively. The application of the HPDE to the various sediment functions was examined using the method described in the next section. In this study, the MPM formula, which is simple and has good applicability, was adopted. Vectors for longitudinal Eq. (2) and transverse Eq. (3) for the sediment flux were assumed based on Watanabe's equation (Watanabe et al., 2001). Equation (7) was used to calculate the Shields number. We derived the steady two-dimensional equation of the water surface profile (Eq. (5), Eq. (6)) to derive the HPDE for the bed level. For details on the derivation process of the steady two-dimensional equation for the water surface profile, please refer to Appendix C.

$$\frac{\partial z}{\partial t} + \frac{1}{1-\lambda}\left(\frac{\partial q_{Bx}}{\partial x} + \frac{\partial q_{By}}{\partial y}\right) = 0 \tag{1}$$

$$q_{Bx} = 8\left(\tau_* - \tau_{*c}\right)^{3/2}\sqrt{sgd^3}\left(\frac{u}{V} - \frac{\gamma^{'}}{\tau_*^{1/2}}\frac{\partial z}{\partial x}\right) \tag{2}$$

$$q_{By} = 8\left(\tau_* - \tau_{*c}\right)^{3/2}\sqrt{sgd^3}\left(\frac{v}{V} - \frac{\gamma^{'}}{\tau_*^{1/2}}\frac{\partial z}{\partial y}\right) \tag{3}$$

$$\gamma^{'} = \sqrt{\frac{\tau_{*c}}{\mu_s \mu_k}} \tag{4}$$

$$\frac{\partial h}{\partial x} = -\frac{\partial z}{\partial x} - I_{ex} - \frac{3}{5}\frac{u^2}{gI_{ex}}\frac{\partial I_{ex}}{\partial x} + \frac{3}{10}\frac{u^2}{gI_e}\frac{\partial I_e}{\partial x} + \frac{2}{5}\frac{uv}{gI_{ey}}\frac{\partial I_{ey}}{\partial y} + \frac{3}{10}\frac{uv}{gI_e}\frac{\partial I_e}{\partial y} - \frac{uv}{gI_{ex}}\frac{\partial I_{ex}}{\partial y} \tag{5}$$

$$\frac{\partial h}{\partial y} = -\frac{\partial z}{\partial y} - I_{ey} - \frac{3}{5}\frac{v^2}{gI_{ey}}\frac{\partial I_{ey}}{\partial y} + \frac{3}{10}\frac{v^2}{gI_e}\frac{\partial I_e}{\partial y} + \frac{2}{5}\frac{uv}{gI_{ex}}\frac{\partial I_{ex}}{\partial x} + \frac{3}{10}\frac{uv}{gI_e}\frac{\partial I_e}{\partial x} - \frac{uv}{gI_{ey}}\frac{\partial I_{ey}}{\partial x} \tag{6}$$

$$\tau_* = \frac{hI_e}{sd} \tag{7}$$

where z is the bed level, t is the time, λ is the porosity of the bed, q_{Bx} is the longitudinal sediment flux, x is the distance of the longitudinal direction, q_{By} is the transverse sediment flux, y is the distance of the transverse direction, τ_* is the composite Shields number, τ_{*c} is the critical Shields number, s is the specific gravity of sediments in water, g is the acceleration due to gravity, d is the sediment size, u is the longitudinal flow velocity, V is the composite flow velocity, v is the transverse flow velocity, μ_s is the coefficient of static friction, μ_s is the coefficient of dynamic friction, and h is the depth. In addition, $I_{bx} = -\partial z/\partial x$ is the longitudinal bed slope, I_{ex} is the longitudinal energy slope, $I_{by} = -\partial z/\partial y$ is the transverse bed slope, and I_{ey} is the transverse energy slope.

First, by applying the chain rule of differentiation to $\partial q_{Bx}/\partial x$ in Eq. (1), we can obtain the following, where n is the coefficient of roughness.

$$\begin{aligned}\frac{\partial q_{Bx}}{\partial x} &= \frac{\partial q_{Bx}}{\partial \tau_*}\left(\frac{\partial \tau_*}{\partial h}\frac{\partial h}{\partial x} + \frac{\partial \tau_*}{\partial I_e}\frac{\partial I_e}{\partial x}\right) \\ &= \frac{\partial q_{Bx}}{\partial \tau_*}\left(\frac{I_e}{sd}\frac{\partial h}{\partial x} + \frac{h}{sd}\frac{\partial I_e}{\partial x}\right) \\ &= \frac{\partial q_{Bx}}{\partial \tau_*}\frac{I_e}{sd}\left(\frac{\partial h}{\partial x} + \frac{h}{I_e}\frac{\partial I_e}{\partial x}\right)\end{aligned} \tag{8}$$

In addition, $\partial I_e/\partial x$ in Eq. (8) becomes the following when the chain rule is applied to differentiate the Manning flow velocity Eq. (9).

$$V = \frac{1}{n}{I_e}^{1/2}h^{2/3} \tag{9}$$

$$\frac{\partial I_e}{\partial x} = \frac{\partial I_e}{\partial h}\frac{\partial h}{\partial x} + \frac{\partial I_e}{\partial V}\frac{\partial V}{\partial x} = -\frac{4}{3}\frac{I_e}{h}\frac{\partial h}{\partial x} + 2\frac{I_e}{V}\frac{\partial V}{\partial x} \tag{10}$$

Substituting Eq. (10) in Eq. (8) and rearranging, we can obtain the following equation.

$$\frac{\partial q_{Bx}}{\partial x} = \frac{\partial q_{Bx}}{\partial \tau_*}\frac{I_e}{sd}\left(-\frac{1}{3}\frac{\partial h}{\partial x} + 2\frac{h}{V}\frac{\partial V}{\partial x}\right) \tag{11}$$

$\partial q_{Bx}/\partial \tau_*$ in the aforementioned equation is given as follows.

$$\frac{\partial q_{Bx}}{\partial \tau_*} = 12\left(\tau_* - \tau_{*c}\right)^{1/2}\sqrt{sgd^3}\left[\frac{u}{V} - \frac{\gamma^{'}}{\tau_*^{1/2}}\left\{1 - \frac{1}{3\tau_*}\left(\tau_* - \tau_{*c}\right)\right\}\frac{\partial z}{\partial x}\right] \tag{12}$$

Equation (5) is used for $\partial h/\partial x$. Substituting Eq. (5) and Eq. (12) in Eq. (11), Eq. (11) becomes the following.

$$\frac{\partial q_{Bx}}{\partial x} = 4\left(\tau_* - \tau_{*c}\right)^{1/2}\sqrt{sgd^3}\left[\frac{u}{V} - \frac{\gamma^{'}}{\tau_*^{1/2}}\left\{1 - \frac{1}{3\tau_*}\left(\tau_* - \tau_{*c}\right)\right\}\frac{\partial z}{\partial x}\right]\frac{I_e}{sd} \left\{\frac{\partial z}{\partial x} + I_{ex} + \frac{3}{5}\frac{u^2}{gI_{ex}}\frac{\partial I_{ex}}{\partial x} - \frac{3}{10}\frac{u^2}{gI_e}\frac{\partial I_e}{\partial x} - \frac{2}{5}\frac{uv}{gI_{ey}}\frac{\partial I_{ey}}{\partial y} - \frac{3}{10}\frac{uv}{gI_e}\frac{\partial I_e}{\partial y} + \frac{uv}{gI_{ex}}\frac{\partial I_{ex}}{\partial y} + 6\frac{h}{V}\frac{\partial V}{\partial x}\right\} \tag{13}$$

In addition, $\partial q_{By}/\partial y$ is arranged in the same process as Eq. (13), and the following equation is obtained.

$$\frac{\partial q_{By}}{\partial y} = 4\left(\tau_* - \tau_{*c}\right)^{1/2}\sqrt{sgd^3}\left[\frac{v}{V} + \frac{\gamma^{'}}{\tau_*^{1/2}}\left\{1 - \frac{1}{3\tau_*}\left(\tau_* - \tau_{*c}\right)\right\}\frac{\partial z}{\partial y}\right]\frac{I_e}{sd} \left\{\frac{\partial z}{\partial y} + I_{ey} + \frac{3}{5}\frac{v^2}{gI_{ey}}\frac{\partial I_{ey}}{\partial y} - \frac{3}{10}\frac{v^2}{gI_e}\frac{\partial I_e}{\partial y} - \frac{2}{5}\frac{uv}{gI_{ex}}\frac{\partial I_{ex}}{\partial x} - \frac{3}{10}\frac{uv}{gI_e}\frac{\partial I_e}{\partial x} + \frac{uv}{gI_{ey}}\frac{\partial I_{ey}}{\partial x} + 6\frac{h}{V}\frac{\partial V}{\partial y}\right\} \tag{14}$$

By substituting Eq. (13) and Eq. (14) in Eq. (1), the following HPDE for bed level z can be derived.

$$\frac{\partial z}{\partial t} + M_x\frac{\partial z}{\partial x} + M_x I_{ex} + M_x F_x + M_y\frac{\partial z}{\partial y} + M_y I_{ey} + M_y F_y = 0 \tag{15}$$

In the aforementioned equation, M_x is the advection velocity of the longitudinal component of bed level z. It is assumed to be closely related to the migrating speed of the longitudinal component of the alternate bars, which is the subject of this study. M_y is the transverse migrating speed of the alternate bars. M_x and M_y are not velocities of the sediments; they are supposed to be the propagation velocities of bed level z. M_x and M_y are given as follows.

$$M_x = \frac{4(\tau_* - \tau_{*c})^{1/2}\sqrt{sgd^3}I_e}{sd(1-\lambda)}\left[\frac{u}{V} - \frac{\gamma^{'}}{\tau_*^{1/2}}\left\{1 - \frac{1}{3\tau_*}\left(\tau_* - \tau_{*c}\right)\right\}\frac{\partial z}{\partial x}\right] \tag{16}$$

$$M_y = \frac{4(\tau_* - \tau_{*c})^{1/2}\sqrt{sgd^3}I_e}{sd(1-\lambda)}\left[\frac{v}{V} - \frac{\gamma^{'}}{\tau_*^{1/2}}\left\{1 - \frac{1}{3\tau_*}\left(\tau_* - \tau_{*c}\right)\right\}\frac{\partial z}{\partial y}\right] \tag{17}$$

Eq. (16) and Eq. (17) indicate that the dominant physical quantities of the migrating speed are I_e, τ_*, and d. In addition, F_x and F_y are given as follows.

$$F_x = \frac{3}{5}\frac{u^2}{gI_{ex}}\frac{\partial I_{ex}}{\partial x} - \frac{3}{10}\frac{u^2}{gI_e}\frac{\partial I_e}{\partial x} - \frac{2}{5}\frac{uv}{gI_{ey}}\frac{\partial I_{ey}}{\partial y} - \frac{3}{10}\frac{uv}{gI_e}\frac{\partial I_e}{\partial y} + \frac{uv}{gI_{ex}}\frac{\partial I_{ex}}{\partial y} + 6\frac{h}{V}\frac{\partial V}{\partial x} \tag{18}$$

$$F_y = \frac{3}{5}\frac{v^2}{gI_{ey}}\frac{\partial I_{ey}}{\partial y} - \frac{3}{10}\frac{v^2}{gI_e}\frac{\partial I_e}{\partial y} - \frac{2}{5}\frac{uv}{gI_{ex}}\frac{\partial I_{ex}}{\partial x} - \frac{3}{10}\frac{uv}{gI_e}\frac{\partial I_e}{\partial x} + \frac{uv}{gI_{ey}}\frac{\partial I_{ey}}{\partial x} + 6\frac{h}{V}\frac{\partial V}{\partial y} \tag{19}$$

4 Verifying the Applications of the HPDE for Bed Level z and the Migrating Speed Formula based on the Measured Values

In this section, we investigate the applicability of the HPDE for bed level z and its calculation formula for the migrating speed derived in the previous section.

4.1 Hydraulics Required to Verify Applicability

This section describes the hydraulic quantities required to verify the applicability of the HPDE and the calculation formula for the migrating speed, as explained in the next section. As demonstrated from the HPDE and the calculation formula for the migrating speed shown in the previous section, the hydraulic quantities required for the verification of the applicability are the water depth, energy slope, and flow velocity. The water depth can be obtained from the bed level and water level measured by the ST. However, the flow velocity and energy slope that are paired with the water depth have not been measured—this measurement is generally difficult. Therefore, we determined the flow velocity and energy slope by performing numerical analyses.

For the numerical analysis, Nays2D, included in iRIC (http://www.i-ric.org), which can solve the two-dimensional plane hydraulic analysis, was employed. The analysis was conducted with a bed level that was measured by the ST as a fixed bed. The spacing of the calculation points was 2 cm, the same as the ST resolution, in both the longitudinal and transverse directions. The upstream boundary condition was the flow rate of 1.5 L/s, and the downstream boundary condition was the measured water depth. The roughness coefficients were adjusted at each time point, such that the calculated values of the water depth and the measured values agreed with each other and were given uniformly throughout the section.

The measured values of the water depth are shown in Fig. 5, the difference between the measured and calculated values of water depth is shown in Fig. 6, which is nondimensionalized by measurement Δh_*, and the calculated values of flow velocity are shown in Fig.7. Of these, Δh_* represents the computational accuracy of the numerical analysis. Considering Δh_* in Fig. 6, Δh_* is generally within 10% for the entire channel at all times, regardless of the development of alternate bars. All the areas where Δh_* was greater than 20% were in very shallow water.

Because Δh_* is nondimensionalized based on the measured values of water depth, it is assumed that Δh_* in this part was calculated to be large. Therefore, it is difficult to determine the computational accuracy of this part by Δh_*. However, if we focus on the calculated values of flow velocity shown in Fig. 7, we can obtain results that are not unnatural as a phenomenon; thus, we decided to use the calculated values of this part as well. In the next section, the applicability of the derived equations is verified using these hydraulic quantities.

4.2 Verifying the Application of the Time Waveform for the Bed Level and the Riverbed Fluctuation Amount

We verified the applicability of the calculation formula derived in the previous section from two viewpoints. First, can the time waveform of the measured bed level be reproduced? Second, can the riverbed fluctuation amount measured in the entire section be reproduced? The verification results are described in this section.

4.2.1 Bed-level Time Waveform

The verification method that uses the time waveform at the bed level is described here. Using the bed level and water depth measured by ST, and the calculated energy gradient and flow velocity from the hydraulic analysis described in the previous section, the HPDE (15) derived in the previous section was numerically integrated, as follows, to calculate the riverbed fluctuation between Δt.

$$\Delta z = \left(-M_x \frac{\partial z}{\partial x} - M_x I_{ex} - M_x F_x - M_y \frac{\partial z}{\partial y} - M_y I_{ey} - M_y F_y \right) \Delta t \tag{20}$$

A time waveform at the bed level was obtained by repeating this numerical integration during each ST measurement time.

The applicability of the HPDE obtained in the previous section was investigated by comparing the time waveform of the bed level. In this study, because the ST measurements were performed at 1-min intervals, Δt in the aforementioned calculation was set to 1 min.

Figure 8 shows the time waveform at the bed level. Figure 8 shows the time waveforms of (a) the left bank side, (b) central part, and (c) right bank side at 6.0 m from the upstream end. The red line shows the bed level of the measured value, and the blue line shows the bed level calculated from the formula.

Comparing the time waveform of the bed level by the calculation formula with the measured value showed that the time waveform of the bed level was well reproduced after 60 min of water flow in figures (a), (b), and (c).

As mentioned earlier, the time waveform was obtained by setting the time integration interval to 1 min. Although this time interval cannot be simply compared, it is much larger than the time interval in general numerical analysis. This result proved that the verification method that uses the aforementioned numerical integration and the applicability of the calculation formula that was derived in the previous section are excellent.

4.2.2 Riverbed Variation Amount

The verification in the previous section showed that the HPDE for Eq. (15) has sufficient applicability; however, its applicability decreased in the early stage of water flow. In this section, we discuss how much of this reduced applicability occupies the entire waterway and where it occurs. This is achieved using the riverbed variation amount. The riverbed variation was verified using the following equation.

$$\Delta z_* = |\Delta z_{obs} - \Delta z_{cal}|/d \times 100 \tag{21}$$

where Δz_{obs} is the riverbed variation obtained from the bed level between the two times that were measured by the ST. In addition, Δz_{cal} is the amount of riverbed variation by the HPDE and the calculation formula of the migrating speed. Δz_* in the aforementioned equation is a dimensionless quantity obtained by dividing the difference between the measured value of the riverbed variation amount and the calculated value using the equation based on the particle size. In addition, the difference between the two shows how much the divergence is based on particle size.

Figure 9 shows a plan view for the calculation accuracy of the riverbed variation Δz_*. Figure 9 shows the bed level, Δz_* from the top. (a) Considering the results for 1 min of water flow, Δz_* is generally within 100%, and the estimation accuracy of the waveform after 1 min at this time is the same as the particle size. From (a) 1 min of water flow to (h) 70 min, we can see that Δz_* is generally within 100% of the entire channel. When focusing on Δz_* from (b) 10 min to (f) 50 min of water flow, areas exceeding 500% occurred periodically in the longitudinal direction, and their total area accounted for approximately 40%. The bed surface at this time showed small irregularities that correspond to the periodically increasing and decreasing Δz_*. Δz_* is within 100% in all intervals because the small irregularities disappear after (g) 60 min. The results of (a) to (g) suggest that the accuracy of the estimation of the calculation formula for the migrating speed decreases when such small irregularities exist on the bed surface. However, the mathematical reason for this is currently unknown. The subject of this study is alternate bars, and it can be said that the authors' equation has sufficient applicability in the case in which alternate bars are dominant.

5 Quantification of the Migrating Speed for the Alternate Bars

The previous section confirmed that the HPDE and calculation formula for the migrating speed can reproduce the propagation phenomenon of alternate bars. In this section, the migrating speed of the alternate bars in each process during the occurrence and development is quantified using the calculation formula of the migrating speed.

5.1 Spatial Distribution of the Migrating Speed of the Alternate Bars

Figure 10 shows a plan view of the dimensionless migrating speed obtained by dividing the migrating speed obtained from the calculation formula for the bed level by the initial uniform flow velocity. The dimensionless migrating speed was used to understand the magnitude of the running water velocity and bed velocity. The above is based on the fact that the governing equations are often nondimensionalized with uniform flow velocities during instability analysis(Callander, 1969; Kuroki & Kishi, 1984).

The figure shows the bed level and M/u_0 from the top. M is the magnitude migrating speed, and u_0 is the uniform flow velocity. The area surrounded by the hatch in the figure is the area in which the Shields number does not exceed the critical Shields number (hereinafter referred to as the effective Shields number); in this area, the migrating speed is 0.

First, by focusing on (a) 1 min of water flow in the figure, M/u_0 has almost no spatial distribution on a floor with an almost flat bed. We also confirmed that the bed surface uniformly propagates at a speed of approximately 0.0015. After the bed changes slightly from (b) 10 min to (e) 40 min, M/u_0 begins to show spatial distribution. Subsequently, the spatial distribution of M/u_0 changes significantly from (g) 60 min of water flow to (l) 110 min. Considering this change with a spatial distribution from place to place, it can be seen that M/u_0 increases at the sedimentary part and the front edge of the alternate bars, and it decreases at other locations.

Next, Fig. 11 illustrates a histogram that quantitatively shows the spatial distribution degree of M/u_0 at each time. The red and blue vertical lines in the figure represent the mean $\pm$ and standard deviation of M/u_0 at each time, and each value is shown at the top of the figure. First, (a) the shape of the histogram after 1 min of water flow is concentrated around an average value of 0.00143. In addition, because the standard deviation is 0.00015, which is small with respect to the mean value, it can be observed that the spatial distribution of M/u_0 at this time was small. Then, from (b) 10 min of water flow to (g) 60 min of water flow when the alternate bars occurred, the shape of the histogram became flat; the mean value of M/u_0 was 0.00126, and the standard deviation was 0.00023. Comparing (a) 1 min and (g) 60 min of water flow showed that although the mean value decreased by approximately 12 %, the standard deviation increased to nearly 1.5 times. This shows that the spatial distribution of the migrating speed greatly expanded from the flat bed to the occurrence of the alternate bars. After that, from (g) 60 min to (l) 110 min of water flow, the flattening of the histogram, the increase in the standard deviation, and the decrease in the mean value of M/u_0 became more significant. Comparing (a) 1 min of water flow and (l) 110 min, which was the final time, showed that the mean value of M/u_0 of (l) is 0.78 times from (a), and the standard deviation of (l) is 2.4 times from (a).

These results demonstrated that the migrating speed of the alternate bars has a spatial distribution, which expands from the stage of occurrence to the development of the alternate bars.

5.2 Scale of the Migrating Speed of the Alternate Bars

This section discusses the scale of the migrating speed of the alternate bars. As shown in the previous section, from Fig. 11, it can be confirmed that the migrating speed has a spatial distribution, which gradually expands from 1 min of water flow to 110 min. The non-dimensional migrating speed in the figure is divided by the uniform flow velocity on the flat floor. The scale of the migrating speed is in the order of 10^{-4} to 10^{-3} of the uniform flow velocity at any location, regardless of the developmental state of the alternate bars. Therefore, it is inferred that the deformation rate of the bed surface is sufficiently smaller than the deformation rate of running water.

6 Applicability of the Formula for Calculating Migrating Speed in Actual Rivers

In section 4, we confirmed that the formula for calculating the migrating speed derived in this study has sufficient applicability in the flume experiment conducted in section 2, and in section 5, the spatial distribution of the migrating speed is quantified. In this section, we investigate the applicability of the formula to an actual river, where the scale, bed material, and hydraulic conditions are completely different from those in the flume experiment.

6.1 Flood Summary for Target River

The study river was the Chikuma River, which flows through Nagano Prefecture, Japan, as shown in Fig. 12(a). It is the longest river in Japan, with a channel length of 300 km. Owing to the outflow of water caused by Typhoon No. 19 in October 2019, the water level remained close to the bank level for approximately 10 h (Fig. 13(b)). This is the largest flow ever recorded and the eighth highest water level ever recorded in the history of observation.

Figure 14(a),(b) are aerial photographs of the river channel before and after the outflow in Ueda City shown in Fig. 12(b). The same figure shows that the alternate bars in the river channel were moved on a large scale by the outflow of water. The light blue line and the blue line in (b) of the same figure show the water route before and after the flood, respectively. Because the position of the water route depends on the position of the alternate bars, the distance moved by the water route at the time of outflow can be considered as the distance moved by the alternate bars before and after the flood, and it can be confirmed that the alternate bars traveled 450 to 800 m during this outflow.

6.2 Hydraulic Analysis for Calculation of Migrating Speed

To calculate the migrating speed obtained using our formula, one-dimensional unsteady flow calculations for a general cross section were performed to calculate the hydraulic quantities required for the calculations. The governing equations used in this calculation are the following two. The reason for the one-dimensional analysis is that it is difficult to obtain detailed information necessary for hydraulic calculations for actual rivers.

$$\frac{\partial A}{\partial t} + \frac{\partial Q}{\partial x} = 0 \tag{22}$$

$$\frac{\partial Q}{\partial t} + \frac{\partial}{\partial x}\left(\frac{Q^2}{A}\right) + gA\frac{\partial}{\partial x}(z+h) + \frac{gn^2 Q|Q|}{R^{4/3}A^2} = 0 \tag{23}$$

where A is the flow area, Q is the flow discharge, t is the time, x is the distance, z is the bed level, h is the water depth, n is Manning's roughness coefficient, and R is the hydraulic mean depth.

The target interval was from the 84-km point at Kuiseshita Observatory to the 109.5-km point at Ikuta Observatory, as shown in Fig. 12(b). For this calculation, we used transect survey data obtained at 500-m intervals and measured in 2017. Notably, from 2017, when the survey was conducted, to 2019, when the water was released, the river had not experienced any water outflow that would have significantly altered the channel geometry. The river bed material was given by varying it as a linear function in the computational section because it was 20 mm at the downstream end and 70 mm at the upstream end of the computational section. The roughness coefficient was given by the Manning–Strickler equation. The upstream boundary condition is the flow discharge at Ikuta Observatory, shown in Fig. 13(a), and the downstream boundary condition is the water level at Kuisenshita Observatory, shown in Fig. 13(b).

Using the hydraulic quantities obtained from the above calculations, the migrating speed was calculated using the following equation. The same equation is a uni-dimensionalized expression obtained by finding the composite component of equations (16) and (17).

$$M = \frac{4(\tau_* - \tau_{*c})^{1/2}\sqrt{sgd^3}I_e}{sd(1-\lambda)}\left(1 - \frac{\gamma^{'}}{\tau_*^{1/2}}\left\{1 - \frac{1}{3\tau_*}\left(\tau_* - \tau_{*c}\right)\right\}\frac{\partial z}{\partial x}\right) \tag{24}$$

6.3 Estimation Result

Fig. 15 shows the longitudinal distribution of the estimated and measured migrating speed, and the same figure shows the interval of the calculation in Fig. 14. The green line in the figure shows the calculation results at each flow discharge marked in Fig. 13, from 1000 m^3/s, when sediment began moving throughout the section, to the peak flow discharge. The migrating speed was calculated using the uni-dimensionalized migrating speed equation shown in equation (24), using the hydraulic mean depth, energy slope, and Shields number. The gray marks in the figure indicate the measured migrating speed. The average migrating speed during the flood period was calculated based on the relationship between the travel distance of the water route and the travel time, which was assumed to be approximately 29 h of active sediment transport based on the flow hydrograph and analysis results.

Focusing on the calculation results of the migrating speed at each flow discharge, we can see that the migrating speed has a spatial distribution at all flow discharge, and it increases as the flow discharge increases.

A comparison of the calculated and measured migrating speeds confirms that the calculated values are about half of the measured values, but they are generally consistent with the measured values, and the waveforms are also generally consistent, except for those at the 104-km point. These results suggest that the hydraulic quantity in the downstream direction is dominant in defining the migrating speed.

7 Discussion

In this section, we discuss the following four aspects of the migrating speed of alternate bars.

7.1 Main Dominant Physical Quantity of Movement Speed

In this study, the migrating speed of alternate bars is quantified by both measurements and estimations. The validity of the calculated migrating speed is also confirmed. In this section, we discuss the mathematical structure of the equation to understand the main dominant physical quantity of the migrating speed.

Fig. 16 shows three relationships between the energy slope, the Shields number, and the dimensionless migrating speed at the final time of the flume experiment. The same figure indicates that the dimensionless migrating speed is proportional to the Shields number and energy slope. Because the dimensionless migrating speed is a product of Shields number and energy slope, it is difficult to say which is dominant. However, in this experiment, the energy slope is closer to the order of the dimensionless migrating speed, indicating that the energy slope is the more dominant physical quantity.

7.2 Approximate Description of Migrating Speed

In the previous section, we showed that the energy slope is the dominant physical quantity that determines the order of migrating speed. From this, it can be inferred that the energy slope can be used to describe the approximate migrating speed. Whether this approximate description is possible was examined based on the relationship between M/u_0 and $0.4 \times I_e$ in Fig. 17. The correlation coefficients between the two at each time are shown in the figure. The value of 0.4 multiplied by the same equation is a coefficient determined from the particle size, which is one of the variables in the denominator of equations (16) and (17).

Considering the relationship between M/u_0 and $0.4 \times I_e$, we can see that the relationship is almost one-to-one at all times. The correlation coefficients are above 0.9 on average, indicating that the two have a strong positive correlation. These results suggest that an approximate description of the migrating speed of alternate bars using energy slope is possible.

7.3 Decreasing Factor for the Migrating Speed of the Alternate Bars

This subsection discusses the decreasing factor for migrating speed of the alternate bars. Figure 18 shows the average longitudinal distributions of the (a) migrating speed, (b) energy line, hydraulic grade line, and bed line over time. The sediment condition for the flume experiment in this study is that no sediment supply exists. Therefore, the bed level and each hydraulic head decreased with time in the upstream section of the moving bed. The water level and energy head in the same section also decreased from the initial stage, and the water surface slope and energy slope, including the riverbed slope, became more moderate. In contrast, the water depth did not change much from the initial value in the whole section. In addition, it can be seen that (a) the migrating speed in the same section decreased from the initial value. Next, if we focus on the point 5.5 m from the upstream end, we can see that the water depth has hardly changed since the initial value, the energy slope has increased, and the migrating speed has also increased.

As shown in Eq. (16) and Eq. (17), there are three dominant physical quantities of the migrating speed, which are grain size, non-dimensional scavenging force, and energy gradient, except for the component decomposition part. The dominant physical quantities of the Shields number are grain size, water depth, and energy slope. Therefore, we can say that there are three physical quantities that effectively govern the migrating speed, which are grain size, water depth, and energy slope. Focusing on these dominant physical quantities, the decreasing factors of the migrating speed of alternate bars in this experiment can be summarized as follows. First, be-

cause the particle size in this experiment is a single particle size, it is assumed that there is no change in the migrating speed due to changes in the particle size. Because the water depth also slightly changed on average, it can be inferred that there was little change in the migrating speed due to changes in the water depth. In contrast, the energy slope was significantly reduced, and the migrating speed was considerably decreased along with it. This decrease in the energy slope is due to the decrease in the bed level caused by the no sediment supply at the upstream end. These results indicate that the reason for the decrease in the migrating speed of the alternate bars in this experiment is the decrease in the energy slope due to the decrease in the bed slope.

Eekhout et al. (Eekhout et al., 2013) observed the occurrence and development processes of alternate bars in an actual river and reported that the bed slope decreased when the migrating speed of alternate bars was decreased. The migrating speed of the alternate bars decreased owing to changes in grain size or water depth because their study had the same target section and the same flood magnitude during the observation period. Based on the results of this experiment, we assumed that the migrating speed decreased owing to the reduction in the energy slope caused by a decrease in the bed slope.

7.4 Comparison of the Migrating Speed of our Method with that of Instability Analysis

The conditions for the occurrence and non-occurrence of alternate bars have been determined by instability analysis for small perturbations given as initial conditions (Callander, 1969; Kuroki & Kishi, 1984). In these instability analyses, the migrating speed of small perturbations was calculated. Although the form of the equation and the process of deriving the equation are different, it can be inferred that the equation for migrating speed based on instability analysis and the equation for migrating speed in this study were essentially the same. In this section, we compare the migrating speed of our method with that of instability analysis.

Fig. 19 shows the relationship between the migrating speed of our method and the migrating speed of instability analysis. The vertical axis of the figure is the migrating speed of our method, which is shown as a box-and-whisker diagram for three time periods: 1 min at the initial river bed, 50 min at the time of sandbar occurrence, and 120 min at the final time under each hydraulic condition shown in Table 1. The horizontal axis of the figure is the migrating speed for the instability analysis and shows the results of each of the linear and weakly nonlinear analyses obtained when the same hydraulic conditions were given as in Table 1. The migrating speed for instability analysis was calculated from the equation proposed by Bertagni et al. (Bertagni & Camporeale, 2018), shown below.

$$M_{*(\mathrm{S.A.:L.})} = -\frac{\mathrm{Im}[\Omega]}{k} \tag{25}$$

$$M_{*(\mathrm{S.A.:W.L.})} = -\left(\frac{\mathrm{Im}[\Omega] - \mathrm{Im}[\Xi]\frac{\mathrm{Im}[\Omega]}{\mathrm{Re}[\Xi]}}{k}\right) \tag{26}$$

where $M_{(\mathrm{S.A.:L.})}$ is the migrating speed from linear instability analysis, $M_{(\mathrm{S.A.:W.L.})}$ is the migrating speed from weakly linear instability analysis, Ω is the amplification factor, k is the wavenumber, and Ξ is the Landau Coefficient. The amplification factor was calculated using the following equation:

$$\Omega = \frac{a_1 + a_2 + a_3 + a_4 + a_5 + a_6}{a_7 + a_8 + a_9 + a_{10}} \tag{27}$$

667

$$a_1 = \frac{i(-1+F_r^2)k_n^2k^3p_d^2\gamma q_{B*0}}{F_r^2\sqrt{\tau_{*0}}\beta} \tag{28}$$

668

$$a_2 = \frac{iC_{f,0}^2(-3+C_d)k_n^2kp_d^2\gamma r\beta q_{B*0}}{\sqrt{\tau_{*0}}} \tag{29}$$

669

$$a_3 = -\frac{k_n^4p_d^4\gamma r\{ik+2C_{f,0}\beta\}q_{B*0}}{F_r^2\sqrt{\tau_{*0}}\beta} \tag{30}$$

670

$$a_4 = -\frac{k^3(k-iC_{f,0}\beta)\{\gamma q_{B*0}(-2+C_d)q_{B*t}\}}{F_r^2} \tag{31}$$

671

$$a_5 = -\frac{1}{F_r^2\sqrt{\tau_{*0}}}k_n^2k^2p_d^2\left[C_{f,0}\{1+(-4+C_d)F_r^2\}\gamma r q_{B*0}+\gamma\sqrt{\tau_{*0}}q_{B*0}(-1+C_dq_{B*t})\right] \tag{32}$$

672

$$a_6 = -\frac{k^3(k-iC_{f,0}\beta)\{\gamma q_{B*0}(-2+C_d)q_{B*t}\}}{F_r^2} \tag{33}$$

673

$$a_7 = \frac{ik_n^2kp_d^2}{F_r^2} \tag{34}$$

674

$$a_8 = \frac{2C_{f,0}k_n^2p_d^2\beta}{F_r^2} \tag{35}$$

675

$$a_9 = -\frac{i(-1+F_r^2)k^2(k-iC_{f,0}\beta)}{F_r^2} \tag{36}$$

676

$$a_{10} = C_{f,0}(-3+C_d)k\beta(k-iC_{f,0}\beta) \tag{37}$$

677 where i is an imaginary unit, F_r is the Froude number, $k_n = m\pi/2$, $m = 1$(alternate
678 bars), $p_d = (-1)^m$, $\gamma = \sqrt{sg\hat{d}^3}/(1-\lambda)\hat{u_0}\hat{h_0}$, s is the specific gravity of sediment
679 in water, $\hat{d}$ is the particle size, g is the gravitational acceleration, λ is the poros-
680 ity, $\hat{u_0}$ is the uniform flow velocity, $\hat{h_0}$ is the uniform flow depth, q_{B*0} is the non-
681 dimensional sediment flux, τ_{*0} is the Shields number, $C_{f,0}$ is the Friction factor at
682 uniform flow, $C_d = 1/C_{f,0}\partial C_f/\partial h$, and $q_{B*t} = \tau_{*0}/q_{B*0}\partial q_{B*}/\partial\tau_*$. Note that sym-
683 bols with ˆ are non-dimensionless numbers, whereas the others are dimensionless. For
684 details, please refer to the original publication (Bertagni & Camporeale, 2018).

685 The migrating speed obtained from the instability analysis is the migrating
686 speed of the dominant wave number during the occurrence of the alternate bars. In
687 contrast, our method provides the migrating speed of alternate bars during each pro-
688 cess from occurrence to development. (a) to (c) in the same figure show the migrat-
689 ing speed of each bar from the time of its occurrence to the development stage. The
690 same figure shows that the migrating speed of our method and that of the instability
691 analysis are of the same scale, regardless of the time of occurrence and the develop-
692 ment stage of the bars.

693 In the previous sections and in Fig. 11, we show that the migrating speed of
694 alternate bars has a spatial distribution and varies with time. Nevertheless, the mi-
695 grating speed of the two types of bars coincided regardless of their developmental
696 stage. Fig. 11 clearly shows that the above reason is that the scale of the change in
697 the migrating speed from occurrence to the development of the alternate bars is very
698 small, and the statistical variance is as small as 10^{-3}.

8 Conclusion

In this study, we first conducted a flume experiment under the condition that alternate bars can occur and develop. We measured the hydraulic quantity and bed shape using a high spatial resolution. Next, we quantified the migrating speed of the alternate bars using the measured values obtained in the flume experiment and the calculation formula. This study determined that the migrating speed of the alternate bars has a spatial distribution, and it changes with time. The results of this study are presented below.

1) We measured the water level and bed level of the occurrence and development process of alternate bars and demonstrated that the migrating speed of the alternate bars has a spatial distribution from the measured geometric shape of the bed surface.
2) The HPDE for bed level z and the formula for the migrating speed were derived to quantitatively determine the migrating speed of the alternate bars. By comparing the measured values with the flume experiment, we demonstrated that the formula can appropriately describe the propagation phenomenon of the alternate bars.
3) By calculating the migrating speed of the alternate bars based on the aforementioned formula, we clarified that the migrating speed of the alternate bars has a spatial distribution. In addition, the spatial distribution changes with the development of bars over time, which was unconfirmed in the literature.
4) We observed that the migrating speed of the alternate bars is about three to four orders of magnitude smaller than the initial uniform flow velocity, regardless of the developmental state and the location of the bars.
5) Our method is generally applicable to actual rivers, where the scale and hydraulic conditions are different from those in the flume experiments.
6) It is suggested that the reason for the decrease in the migrating speed of the alternate bars is the decrease in the energy slope due to the decrease in the bed slope.
7) The migrating speeds of our method and the instability analysis generally agreed with each other. One of the reasons for this is that the statistical variance of the migrating speed, which was calculated in the flume experiment conducted in this study, was small.

Acknowledgments

The data used in this study can be accessed at (https://doi.org/10.4121/16788778.v1). For details of the data, please refer to the enclosed README.md. This work was supported by JSPS KAKENHI Grant Numbers JP21H04596, JP20K20543, and JICE(No.19005 and No. 20004), Japan Institute of Country-ology and Engineering. The contents of this paper have been greatly improved by the comments of the reviewers. I also used the Mathematica code provided in Supporting Information in Bertagni et al.'s paper (Bertagni & Camporeale, 2018), with input from reviewer Bertagni, to improve the content. We would like to express our gratitude for these contributions. We would like to express our gratitude. We would like to thank Editage (www.editage.com) for English language editing.

References

Adami, L., Bertoldi, W., & Zolezzi, G. (2016). Multidecadal dynamics of alternate bars in the alpine rhine river. *Water Resources Research*, *52*(11), 8938-8955. doi: https://doi.org/10.1002/2015WR018228

Bertagni, M. B., & Camporeale, C. (2018). Finite amplitude of free alternate bars

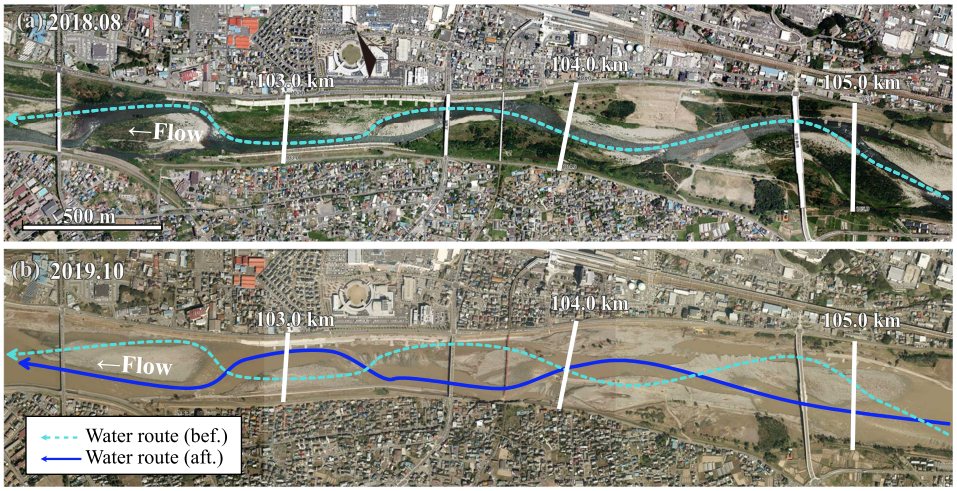

Figure 1. Aerial photos of the Chikuma river of Japan (a) before the flood, (b) after the flood (「Part 2 Chikumagawa teibou chousa iinnkai shiryou」(Ministry of Land, Infrastructure, Transport and Tourism) (https://www.hrr.mlit.go.jp/river/chikumagawateibouchousa/chikuma-02.pdf) created by processing).

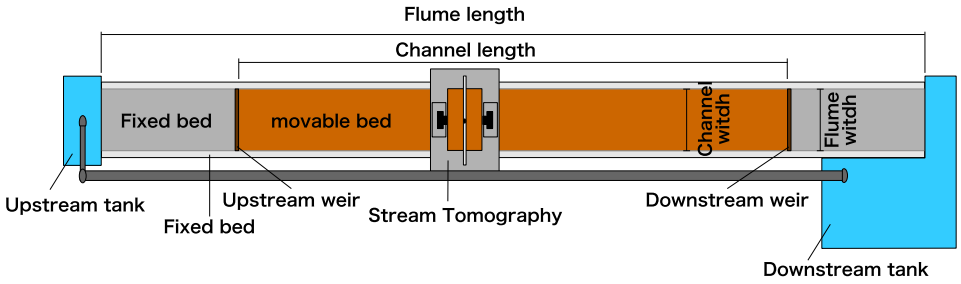

Figure 2. Plan view of the experimental flume.

with suspended load. *Water Resources Research*, *54*(12), 9759-9773. doi: https://doi.org/10.1029/2018WR022819

Callander, R. A. (1969). Instability and river channels. *Journal of Fluid Mechanics*, *36*(3), 465-480. doi: 10.1017/S0022112069001765

Colombini, M., Seminara, G., & Tubino, M. (1987). Finite-amplitude alternate bars. *Journal of Fluid Mechanics*, *181*, 213-232. doi: 10.1017/S0022112087002064

Colombini, M., & Tubino, M. (1991). Finite-amplitude free bars: A fully nonlinear spectral solution. *in Sand Transport in Rivers, Estuaries and the Sea, edited by R. Soulsby and R. Bettes*, *A. A. Balkema, Brookfield, Vt.*, 163-169.

Crosato, A., Desta, F. B., Cornelisse, J., Schuurman, F., & Uijttewaal, W. S. J. (2012). Experimental and numerical findings on the long-term evolution of migrating alternate bars in alluvial channels. *Water Resources Research*, *48*(6). doi: 10.1029/2011WR011320

Crosato, A., Mosselman, E., Beidmariam Desta, F., & Uijttewaal, W. S. J. (2011). Experimental and numerical evidence for intrinsic nonmigrating bars in alluvial channels. *Water Resources Research*, *47*(3). doi: 10.1029/2010WR009714

Eekhout, J. P. C., Hoitink, A. J. F., & Mosselman, E. (2013). Field experiment on alternate bar development in a straight sand-bed stream. *Water Resources Research*, *49*(12), 8357-8369. doi: 10.1002/2013WR014259

Federici, B., & Seminara, G. (2003). On the convective nature of bar instability.

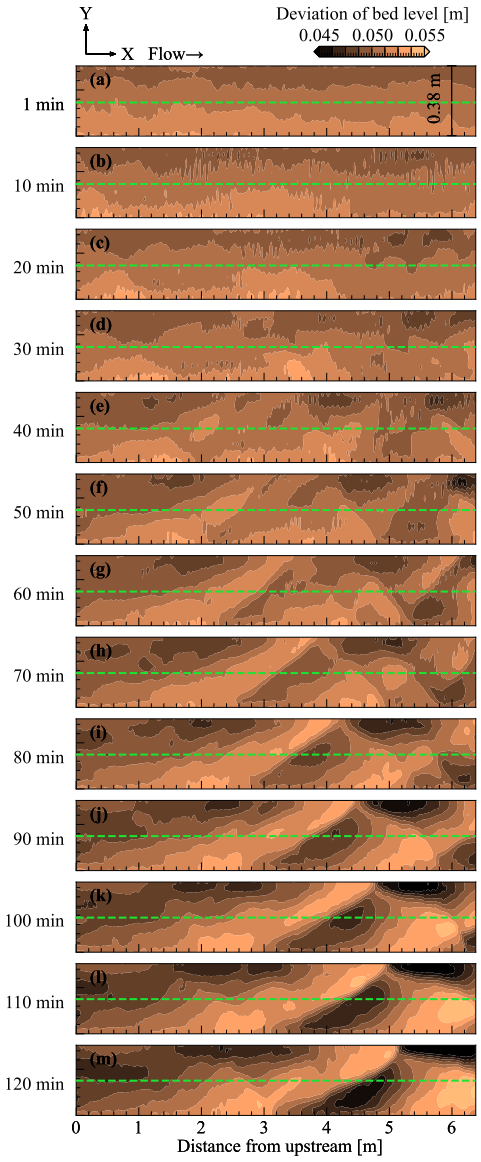

Figure 3. Temporal changes of the plan view in the observed bed topography.

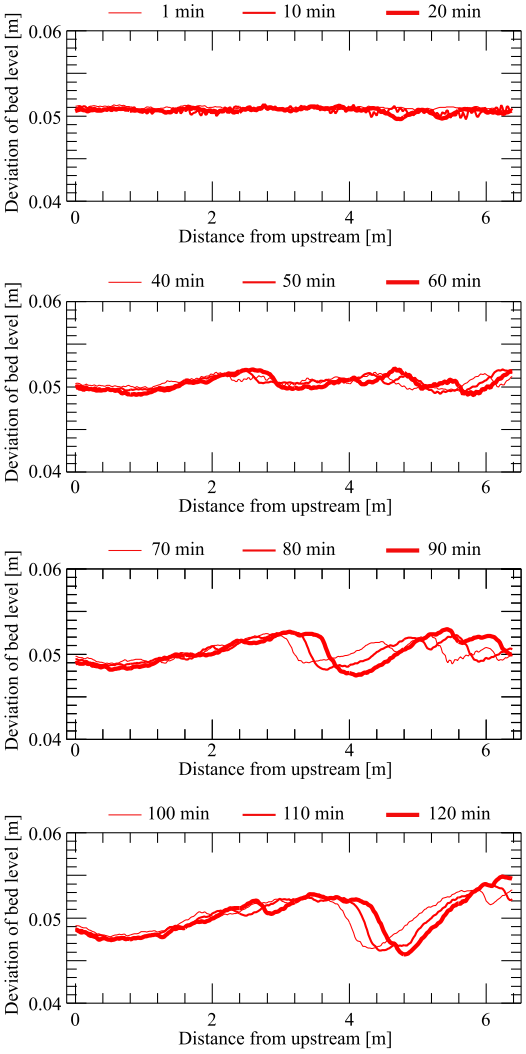

Figure 4. Longitudinal view of the measured bed shape: (a) Initial stage of the experiment, (b) occurrence of alternate bars, (c) intermediate stage of the experiment, and (d) final stage of the experiment.

Journal of Fluid Mechanics, *487*, 125-145. doi: 10.1017/S0022112003004737

Fujita Y., F. R. M. Y., Koike T. (1985). Experiments on the initial stage of alternate bar formation. *Disaster Prevention Research Institute Annuals (in Japanese)*, *28*(B-2), 379-398.

Hiroshi, I. (1983). Experiments on bedload transport,bed forms,and sedimentary structures using fine gravel in the 4-meter-wide flume..

Hoshino, T., Yasuda, H., & Kurahashi, M. (2018). Direct measurement method of formation processes of alternate bars. *J. Jpn. Soc. Civ. Eng. Ser. Applied Mechanics.(in Japanese)*, *A2. 74(1)*, 63-74.

Kennedy, J. F. (1963). The mechanics of dunes and antidunes in erodible-bed channels. *Journal of Fluid Mechanics*, *16*(4), 521-544. doi: 10.1017/S0022112063000975

Kinoshita, R. (1958). Experiment on dune length in straight channel. *Journal of*

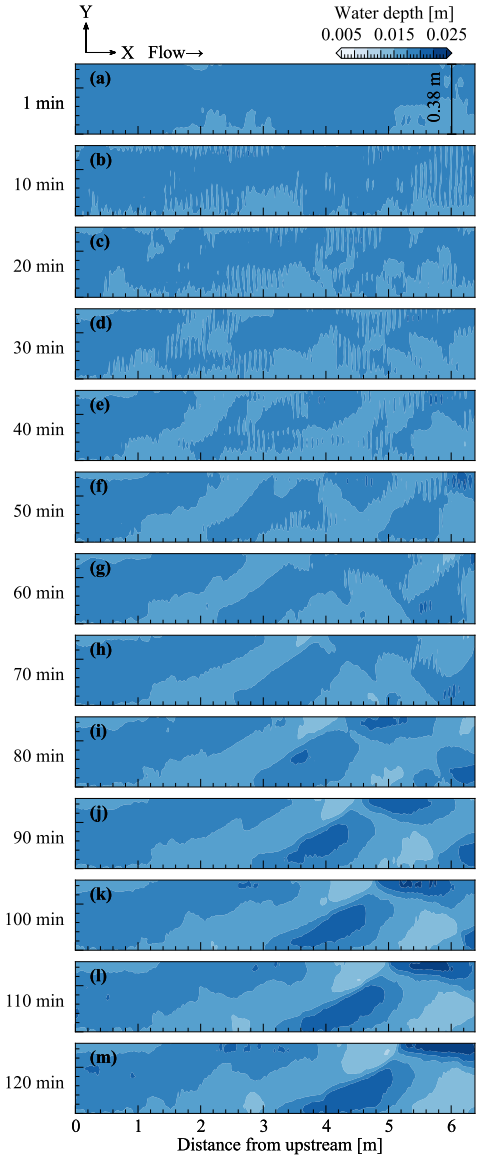

Figure 5. Temporal changes in the plan view for the observed water depth.

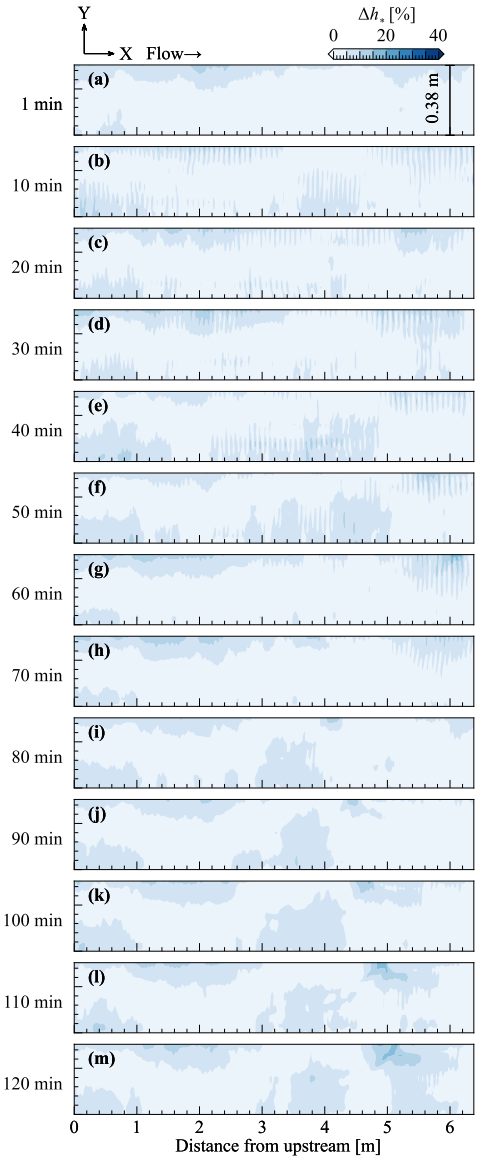

Figure 6. Difference between the measured and calculated values of the water depth that is made dimensionless using the measured value.

the Japan Society of Erosion Control Engineering (in japanese), *1958*(30), 1-8. doi: 10.11475/sabo1948.1958.30_1

Kinoshita, R. (1961). Investigation of channel deformation in ishikari river. *Rep. Bureau of Resources, Dept. Science & Technology, Japan. (in japanese)*.

Kuroki, M., & Kishi, T. (1984). Regime criteria on bars and braids in alluvial straight channels. *Proceedings of the Japan Society of Civil Engineers*, *1984*(342), 87-96. doi: 10.2208/jscej1969.1984.342_87

Lanzoni, S. (2000a). Experiments on bar formation in a straight flume: 1. uniform sediment. *Water Resources Research*, *36*(11), 3337-3349. doi: 10.1029/2000WR900160

Lanzoni, S. (2000b). Experiments on bar formation in a straight flume: 2. graded

sediment. *Water Resources Research*, *36*(11), 3351-3363. doi: 10.1029/2000WR900161

Miwa, H., Daisdo, A., & Katayama, T. (2007). Effects of water and sediment discharge conditions on variation in alternate bar morphoroly. *Proceedings of hydraulic engineering (in japanese)*, *51*, 1051-1056. doi: 10.2208/prohe.51.1051

Nelson, P., & Morgan, J. (2018, 09). Flume experiments on flow and sediment supply controls on gravel bedform dynamics. *Geomorphology*, *323*. doi: 10.1016/j.geomorph.2018.09.011

Nobuhisa, N., Yoshio, M., Yoshihiko, U., Takashi, H., Masayuki, Y., Yasuhiko, T., & Michiaki, I. (1999). On the behaviour of alternate bars under several kinds of channel conditions. *PROCEEDINGS OF HYDRAULIC ENGINEERING (in japanese)*, *43*, 743-748.

Norihiro, I., & Adichai, P. (2002). Weakly nonlinear analysis of bars with the use of the amplitude expansion method. *Doboku Gakkai Ronbunshu*, *2002*(712), 73-86. doi: 10.2208/jscej.2002.712_73

Podolak, C. J. P., & Wilcock, P. R. (2013). Experimental study of the response of a gravel streambed to increased sediment supply. *Earth Surface Processes and Landforms*, *38*(14), 1748-1764. doi: 10.1002/esp.3468

Schielen, R., Doelman, A., & Swart, H. E. (1993). On the nonlinear dynamics of free bars in straight channels. *Journal of Fluid Mechanics*, *252*, 325-356.

Seminara, G. (2010). Fluvial sedimentary patterns. *Annual Review of Fluid Mechanics*, *42*(1), 43-66. doi: 10.1146/annurev-fluid-121108-145612

Shimizu, Y., & Itakura, T. (1989). Calculation of bed variation in alluvial channels. *Journal of Hydraulic Engineering*, *115*(3), 367-384. doi: 10.1061/(ASCE)0733-9429(1989)115:3(367)

Tubino, M. (1991). Growth of alternate bars in unsteady flow. *Water Resources Research*, *27*(1), 37-52. doi: 10.1029/90WR01699

Venditti, J. G., Nelson, P. A., Minear, J. T., Wooster, J., & Dietrich, W. E. (2012). Alternate bar response to sediment supply termination. *Journal of Geophysical Research: Earth Surface*, *117*(F2). doi: 10.1029/2011JF002254

Watanabe, A., Fukuoka, S., Yasutake, Y., & Kawaguhi, H. (2001). Groin arrangements made of natural willows for reduceing bed deformation in a curved channel. *Advances in river engineering (in japanese)*, *7*, 285-290.

Yuichi, I. (1956). Hydrodynamical study on critical tractive force. *Transactions of the Japan Society of Civil Engineers (in Japanese)*, *1956*(41), 1-21. doi: 10.2208/jscej1949.1956.41_1

Yuichiro, F., & Yoshio, M. (1985). Studies on the process of development of alternate bars. *Bulletin of the Disaster Prevention Research Institute*, *30(3)*, 55-86.

Zhang, Z. (1998). Flexible new technique for camera calibration. *Technical Report MSR-TR-98-71, Microsoft Research, Microsoft Corporation*.

Appendix A Stream Tomography

Here, we describe the measurement principle of the stream tomography used in the flume experiment.

A1 Outline of the Measurement Device and Measurement Procedure

Figure A1 and Fig. A2 show the overall plan view of the measurement device and the layout of the equipment. The overall configuration of the measurement device includes a laser sheet light source and a traveling platform that has two digital cameras installed. The laser sheet light source used in this study is a yttrium aluminum garnet (YAG) laser with a wavelength of 532 nm. In addition, to promote

the emission of the laser light in water, the water used in the flume experiment was green because of dissolved sodium fluorescein. As shown in Fig. A1 and Fig. A2, the two digital cameras sandwiched the laser sheet light source so it was upstream and downstream on the traveling platform. The camera was installed such that it was diagonally downward toward the center of the stream. The three-dimensional coordinates of the water level and bed level by the ST can be obtained based on the intersection of the origin coordinates (lens center point) for each of the two aforementioned cameras and the geometric vector that connects the water level and bed position that will be measured.

A2 Physical principles

This measurement method is based on the principle of triangulation, in which three-dimensional coordinates are obtained from the intersection of two geometric vectors connecting two known points and a measurement target. In this study, the vectors of the directed line segments are referred to as geometric vectors. The geometric relationship in this method is shown in Fig. A3. The water surface level can be calculated as the intersection h of two geometric vectors connecting the origin coordinates of each of the two cameras and the laser reflection coordinates of the water surface, and the water bottom level is calculated as the intersection b of two geometric vectors connecting the water surface level and the laser reflection coordinates of the water bottom level. Of these, the calculation of the 3-D coordinates of the water bottom level requires consideration of refraction at the water surface. In this method, the refraction of the reflected laser beam at the bottom of the water surface is corrected based on Snell's law, and the 3-D coordinates of the bottom level are obtained based on the water surface level that can be obtained areally. The measurement procedure comprises the following four steps: 1) video recording with two cameras while the carriage is moving in the downstream direction, 2) analysis of the intersection points between the laser sheet and the water/bed surface in the videos, 3) calculation of the water surface level h based on triangulation, and 4) calculation of the bed level b by correction based on Snell's law. The internal and external parameters of the camera required as the origin of the calculation were calculated using Zhang's calibration method (Zhang, 1998). The origin coordinates of the two cameras were calculated for upstream C_u and downstream C_d, respectively. C_u and C_d are number vectors with 3-D spatial coordinates as components, $C_u = (x_{c_u}, y_{c_u}, z_{c_u})$ and $C_d = (x_{c_d}, y_{c_d}, z_{c_d})$.

A3 Image analysis

To measure the geometries of the water surface and the water bottom, pixel numbers corresponding to the water surface and bed surface were detected in the captured images. i and j represent the pixel numbers in the horizontal and vertical directions of the image, respectively. The pixel number corresponding to the intersection of the laser sheet and the water surface was detected using Canny, a function of OpenCV(https://opencv.org), and by specifying the green lightness range as the threshold. Similarly, the pixel number corresponding to the intersection of the laser sheet and the bed surface was detected as the maximum value of the green lightness in the j-direction. The reflectance intensity of the green luminosity at the water surface and bottom varies depending on the experimental environment, the intensity of the laser beam, and the riverbed material. In particular, the detection threshold of the water surface must be adjusted according to the measurement conditions. In this study, the water surface detection threshold was set to a range in which the green luminosity exceeded 40 but did not exceed 160.

A4 Obtaining the water surface gradient for refraction correction

This subsection presents a procedure for calculating the water surface gradient required for the calculation of the bed level by refraction correction based on Snell's law, using a grid of water surface measurements. Numerous water surface measurements can be conducted in the longitudinal and transverse directions with the spatial resolution described above. Because a gradient of the water surface is required for refraction correction of the bed surface measurement, a structured discrete function $H_{(i,j)}$ is created by arranging h in Fig. A3 in a grid of arbitrary intervals (Fig. A4). The bed level b was calculated from the geometric relationship shown in Fig. A5. Accurate refraction correction requires C_{hu} and C_{hd}, as shown in Fig. A5, and the water surface slope (normal vector of the water surface) n_u and n_d at that point. $C_{hu}(C_{hd})$ is the intersection vector between, the vector connecting $C_u(C_d)$ and the identified pixel at the bottom, and the water surface. Because $n_u(n_d)$ represents the water surface gradient at $C_{hu}(C_{hd})$, it can be calculated using $H_{(i,j)}$. The refractive indices used for refraction correction were air ($n_{air} = 1.0$) and water ($n_{water} = 1.333$), respectively.

A5 Validation

The following experiments were conducted to verify the accuracy and applicability of ST. Experiments 1 to 3 were conducted without sand, using objects of known shapes (Fig. A6), and Experiment 4 was conducted in a flow over a sand wave of the scale often observed in experiments on sandbars. To verify the accuracy of measurement, the plane of the rectangular top surface placed on the bottom was used, as shown in Fig. A6, because the true value shape of the flume bottom was unknown. The measurement principle of ST is such that the measurement error becomes large when the geometric shape of the bottom surface abruptly changes in the longitudinal direction, and a blind spot exists in the view of the camera. Therefore, hemispheres were used for verification to confirm the follow-up of the measurements in the longitudinal direction. The hemisphere has an infinite divergence of bed slope at the point of contact with the bottom. The size of the hemisphere was $r = 2.5$ cm, which is larger than the maximum wave height of the sand waves (=2 cm), as confirmed in the preliminary experiments. The flow depth in experiments 1 to 3 was set to be 1.5 to 4 cm in the measurement range, which is a condition for the hemisphere to be underwater. The flow depth in the experiments on sand bars in this flume was approximately 1 to 3 cm. In Experiment 4, the bottom of the channel was covered with 5 cm of silica sand ($D_{50} = 0.755$ mm), which is commonly used in moving-bed experiments, and the discharge was 2.5 l/sec for 2 h to confirm the formation of sandbars. Subsequently, the sandbar was drained and fixed with cement.

A6 Experiment 1 (dry)

The purpose of Experiment 1 was to verify the validity of the triangulation-based ST and its angular tracking capability.

In the upper part of Fig. A7, the plane of the rectangle was measured five times, and the measurement results are shown in three measurement lines for the longitudinal and transverse directions. The lines were set at 3 cm intervals for both longitudinal and transverse measurements. The upper solid line in Fig. A7 is an estimate obtained from the least-squares method of the measurement results and is regarded as the true value in the evaluation of this section. The true value lines are skewed in both longitudinal and transverse sections, but this is due to the skewness of the measuring device or the water channel and is unrelated to the measurement accuracy. The measurement error of the triangulation is shown by the difference from the true value in the lower part of Fig. A7. The error of the measurement was

less than 0.03 cm at all measurement points in each longitudinal and transverse direction.

To verify the angular-tracking properties, Fig. A8 shows the measurement results of three hemispheres lined up in the longitudinal direction and the solid line of the true value superimposed. The measurement results are shown by superimposing the results of five measurements in three hemispheres (15 measurements in total). The vertical error of each measurement is shown on the right side of Fig. A8. While the error was less than 0.1 cm near the hemisphere apex, the accuracy deteriorated as the angle to the bottom increased or decreased. Using an error of 0.2 cm as a threshold, the following angle was calculated to be approximately 60°, which is consistent with the camera's overhead angle. The accuracy is lower for hemispheres than for rectangles because the timing of the camera shots cannot be perfectly matched.

A7 Experiment 2 (Still water)

Experiment 2 was conducted to verify the validity of the ST water surface measurements and bottom measurements with refraction correction.

In the upper part of Figs. A9,A10, the measurement results of the hydrostatic surfaces of three measurement lines in the longitudinal and transverse directions and the estimated values obtained by the least-squares method as true values as in A6 are shown as solid lines. The position of the measurement line in the transverse direction was $x = 100, 200, 300$ cm with $x = 0$ cm as the starting point. The position of the measurement line in the longitudinal direction was $y = 7.5, 22.5, 37.5$ cm with $y = 0$ cm on the right bank of the channel. The error from the true value is shown in the lower part of Figs. A9,A10. The measurement results include a characteristic error which seems to be affected by the movement of the carriage, but the cause remains unknown. Figs. A11,A12 show the histograms of the errors in the longitudinal and transverse directions of the water surface, respectively, with the sum of the three lateral segments. The magnitude of the error varies depending on the location, but it is less than 0.05 cm for most of the longitudinal transects and about 0.1 cm at the maximum.

Fig. A13 shows the measurement results of the hemisphere in still water and the solid line of the true value, as in Subsection A6, overlaid with results of 15 measurements. The measurement of the bottom surface in still water requires refraction correction based on the measured values at the water surface, but there was no degradation in accuracy. In addition, the angular follow-up was approximately the same.

A8 Experiment 3 (Flowing water)

Experiment 3 was conducted to verify the validity of the measurements under flowing water conditions. Fig. A14 shows the measurement results of the hemisphere at the bottom of the flowing water condition and the solid line of the true value, superimposed with the results of 15 measurements as in Subsection A6. The measurement accuracy and angular follow-up remained almost unchanged from those in the dry and still water conditions.

Appendix B Validity of the Pseudo-steady Flow Assumption Applied to Bars-Scale Riverbed Waves

This section describes the validity of the pseudo-steady flow assumption applied to the bar-scale riverbed waves. In this study, we introduced the assumption

of a pseudo-steady flow when deriving the HPDE for bed level z. This assumption is often introduced in stability analyses of bar-scale riverbed waves(Callander, 1969; Kuroki & Kishi, 1984). In the aforementioned stability analysis, we assumed that the migrating speed of the bed is sufficiently slower than the propagation velocity of the flow, and the flow can be treated as a pseudo-steady flow if the flow rate is constant. Based on this assumption, for stability analysis, we ignore the term of the time gradient in the continuity equation of flow and the equation of motion of flow among the governing equations that are used in the analysis. The aforementioned assumptions are considered to be valid. This is because the stability analysis explains the occurrence and developmental mechanisms of alternate bars. However, to the best of our knowledge, whether the term of the time gradient of the flow can actually be ignored cannot be confirmed from the actual phenomenon. Therefore, we verified whether the term of the flow time gradient can be ignored with ST measurement values and hydraulic analysis.

The aforementioned verification was performed by comparing the contributions of each term in the equation of motion for flow.

$$\frac{1}{g}\frac{\partial u}{\partial t} + \frac{u}{g}\frac{\partial u}{\partial x} + \frac{\partial H}{\partial x} + I_{ex} = 0 \tag{B1}$$

where H is the water level. As the explanation of the various physical quantities has already been provided, it is omitted here. The contribution of each term in the aforementioned equation was calculated for each ST measurement time, and the magnitudes were compared.

$\partial H/\partial x$ was obtained with the measured value of the water level of the ST. Other terms were obtained with the results of the hydraulic analysis, which is described in Section 4.1 in the main text. The time interval and spatial interval of the calculation were 1 min and 2 cm, respectively, which are the time resolutions and spatial resolutions of ST. The flow velocity and migrating speed of the y component under the experimental conditions were 10^{-4} to 10^{1} of the x components at any location regardless of the developmental state of the alternate bars. For simplicity, the y component is ignored in this section.

Figure B1 shows the time change of the box-beard diagram that displays the contribution of each term. This figure shows the (a) local term, (b) advection term, (c) pressure term, and (d) friction term, which correspond to the order of each term in Eq. (B1). The figure shows that although the (b) advection term, (c) pressure term, and (d) friction term dominate the flow at any time, it can be confirmed that (a) the local term can be ignored because it is smaller than the aforementioned three terms. Even if the advection term with the smallest contribution in (b), (c), and (d) is compared with the local term, the contribution of the local term is 10^{-4} to 10^{-2} of the (b) advection term. In addition, it can be observed that the local term is extremely small. From this, it is inferred that it is physically appropriate to ignore the time gradient of flow in the alternate bars.

Appendix C Derivation of the Two-Dimensional Equation of the Water Surface Profile

Appendix C presents the derivation processes of the two-dimensional equation of the water surface profile to derive the HPDE for the bed level. The governing equations used for the derivation consist of the following continuous equations and the equations of motion. When deriving the equation, the flow can be treated as a pseudo-steady-state flow based on the verification results in Appendix B. Therefore, the following continuous equations and equations of motion were used for the deriva-

tion.

$$\frac{\partial[hu]}{\partial x}+\frac{\partial[hv]}{\partial y}=0 \tag{C1}$$

$$\frac{u}{g}\frac{\partial u}{\partial x}+\frac{v}{g}\frac{\partial u}{\partial y}+\frac{\partial z}{\partial x}+\frac{\partial h}{\partial x}+I_{ex}=0 \tag{C2}$$

$$\frac{u}{g}\frac{\partial v}{\partial x}+\frac{v}{g}\frac{\partial v}{\partial y}+\frac{\partial z}{\partial y}+\frac{\partial h}{\partial y}+I_{ey}=0 \tag{C3}$$

As an explanation of the various physical quantities has already been provided, it is omitted here.

The derivation of $\partial h/\partial x$ is described as follows. First, applying the product rule to Eq. (C1) results in the following equation.

$$h\frac{\partial u}{\partial x}+u\frac{\partial h}{\partial x}+h\frac{\partial v}{\partial y}+v\frac{\partial h}{\partial y}=0 \tag{C4}$$

Next, for the first and third terms on the left side of Eq. (C4),

$$u=\frac{1}{n}\frac{I_{ex}}{I_e^{1/2}}h^{2/3} \tag{C5}$$

$$v=\frac{1}{n}\frac{I_{ey}}{I_e^{1/2}}h^{2/3} \tag{C6}$$

$$\frac{\partial u}{\partial x}=\frac{\partial u}{\partial h}\frac{\partial h}{\partial x}+\frac{\partial u}{\partial I_{ex}}\frac{\partial I_{ex}}{\partial x}+\frac{\partial u}{\partial I_e}\frac{\partial I_e}{\partial x}=\frac{2}{3}\frac{u}{h}\frac{\partial h}{\partial x}+\frac{u}{I_{ex}}\frac{\partial I_{ex}}{\partial x}-\frac{1}{2}\frac{u}{I_e}\frac{\partial I_e}{\partial x} \tag{C7}$$

$$\frac{\partial v}{\partial y}=\frac{\partial v}{\partial h}\frac{\partial h}{\partial y}+\frac{\partial v}{\partial I_{ey}}\frac{\partial I_{ey}}{\partial y}+\frac{\partial v}{\partial I_e}\frac{\partial I_e}{\partial y}=\frac{2}{3}\frac{v}{h}\frac{\partial h}{\partial y}+\frac{v}{I_{ey}}\frac{\partial I_{ey}}{\partial y}-\frac{1}{2}\frac{v}{I_e}\frac{\partial I_e}{\partial y} \tag{C8}$$

After differentiating the composite function (Eq. (C7) and Eq. (C8)) using Manning's flow velocity formula (Eq. (C5), Eq. (C6)), substituting it into Eq. (C4), and rearranging $\partial h/\partial x$, the following equation is obtained.

$$\frac{\partial h}{\partial x}=-\frac{3}{5}\frac{h}{I_{ex}}\frac{\partial I_{ex}}{\partial x}+\frac{3}{10}\frac{h}{I_e}\frac{\partial I_e}{\partial x}-\frac{v}{u}\frac{\partial h}{\partial y}-\frac{3}{5}\frac{vh}{uI_{ey}}\frac{\partial I_{ey}}{\partial y}+\frac{3}{10}\frac{vh}{uI_e}\frac{\partial I_e}{\partial y} \tag{C9}$$

Next, after substituting Eq. (C7) and the following Eq. (C10) into the first and second terms of the equation of motion in the x direction for Eq. (C2), we get

$$\frac{\partial u}{\partial y}=\frac{\partial u}{\partial h}\frac{\partial h}{\partial y}+\frac{\partial u}{\partial I_{ex}}\frac{\partial I_{ex}}{\partial y}+\frac{\partial u}{\partial I_e}\frac{\partial I_e}{\partial y}=\frac{2}{3}\frac{u}{h}\frac{\partial h}{\partial y}+\frac{u}{I_{ex}}\frac{\partial I_{ex}}{\partial y}-\frac{1}{2}\frac{u}{I_e}\frac{\partial I_e}{\partial y} \tag{C10}$$

After substituting Eq. (C9), which was organized earlier into Eq. (C11), we get

$$\begin{aligned}\frac{2}{3}\frac{u^2}{gh}\frac{\partial h}{\partial x}+\frac{u^2}{gI_{ex}}\frac{\partial I_{ex}}{\partial x}-\frac{1}{2}\frac{u^2}{gI_e}\frac{\partial I_e}{\partial x}+\frac{2}{3}\frac{uv}{gh}\frac{\partial h}{\partial y}\\ +\frac{uv}{gI_{ex}}\frac{\partial I_{ex}}{\partial y}-\frac{1}{2}\frac{uv}{gI_e}\frac{\partial I_e}{\partial y}+\frac{\partial z}{\partial x}+\frac{\partial h}{\partial x}+I_{ex}=0\end{aligned} \tag{C11}$$

The following equation can be obtained by rearranging $v/u\partial h/\partial y$.

$$\begin{aligned}\frac{v}{u}\frac{\partial h}{\partial y}=\frac{3}{5I_{ex}}\left(\frac{u^2}{g}-h\right)\frac{\partial I_{ex}}{\partial x}+\frac{3}{10I_e}\left(-\frac{u^2}{g}+h\right)\frac{\partial I_e}{\partial x}\\ +\frac{1}{5I_{ey}}\left(-\frac{2uv}{g}-\frac{3vh}{u}\right)\frac{\partial I_{ey}}{\partial y}+\frac{3}{10I_e}\left(-\frac{uv}{g}+\frac{vh}{u}\right)\frac{\partial I_e}{\partial y}+\frac{uv}{gI_{ex}}\frac{\partial I_{ex}}{\partial y}+\frac{\partial z}{\partial x}+I_{ex}\end{aligned} \tag{C12}$$

After substituting Eq. (C12) into Eq. (C9) and rearranging it, the following $\partial h/\partial x$ is derived.

$$\frac{\partial h}{\partial x} = -\frac{\partial z}{\partial x} - I_{ex} - \frac{3}{5}\frac{u^2}{gI_{ex}}\frac{\partial I_{ex}}{\partial x} + \frac{3}{10}\frac{u^2}{gI_e}\frac{\partial I_e}{\partial x} + \frac{2}{5}\frac{uv}{gI_{ey}}\frac{\partial I_{ey}}{\partial y} + \frac{3}{10}\frac{uv}{gI_e}\frac{\partial I_e}{\partial y} - \frac{uv}{gI_{ex}}\frac{\partial I_{ex}}{\partial y} \quad \text{(C13)}$$

By rearranging $\partial h/\partial y$ using the same process as before, the following equation for $\partial h/\partial y$ is obtained.

$$\frac{\partial h}{\partial y} = -\frac{\partial z}{\partial y} - I_{ey} - \frac{3}{5}\frac{v^2}{gI_{ey}}\frac{\partial I_{ey}}{\partial y} + \frac{3}{10}\frac{v^2}{gI_e}\frac{\partial I_e}{\partial y} + \frac{2}{5}\frac{uv}{gI_{ex}}\frac{\partial I_{ex}}{\partial x} + \frac{3}{10}\frac{uv}{gI_e}\frac{\partial I_e}{\partial x} - \frac{uv}{gI_{ey}}\frac{\partial I_{ey}}{\partial x} \quad \text{(C14)}$$

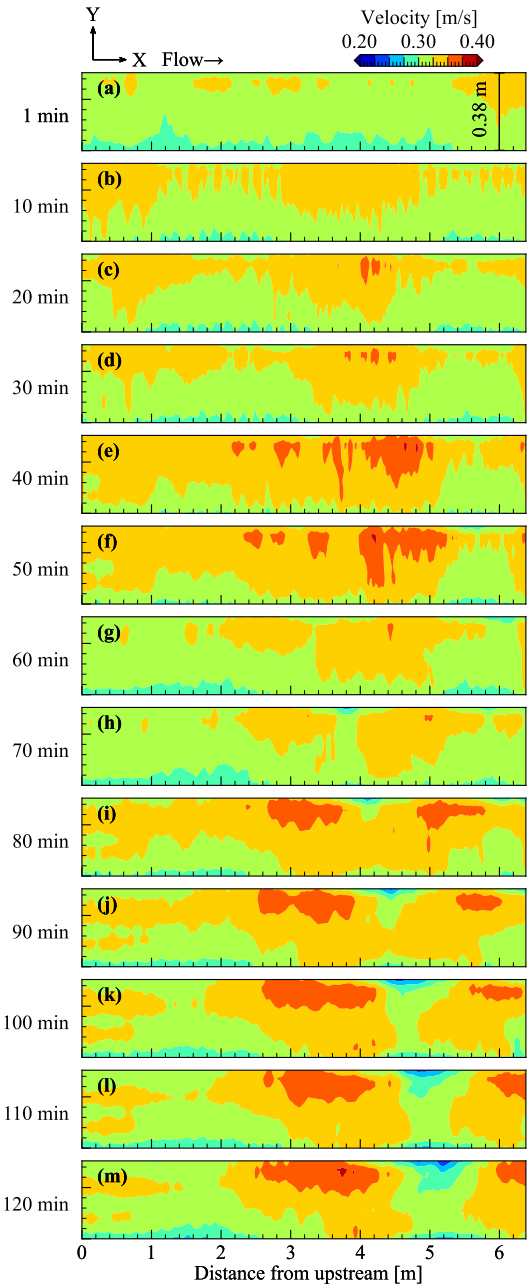

Figure 7. Temporal changes in the plan view for the calculated flow velocity.

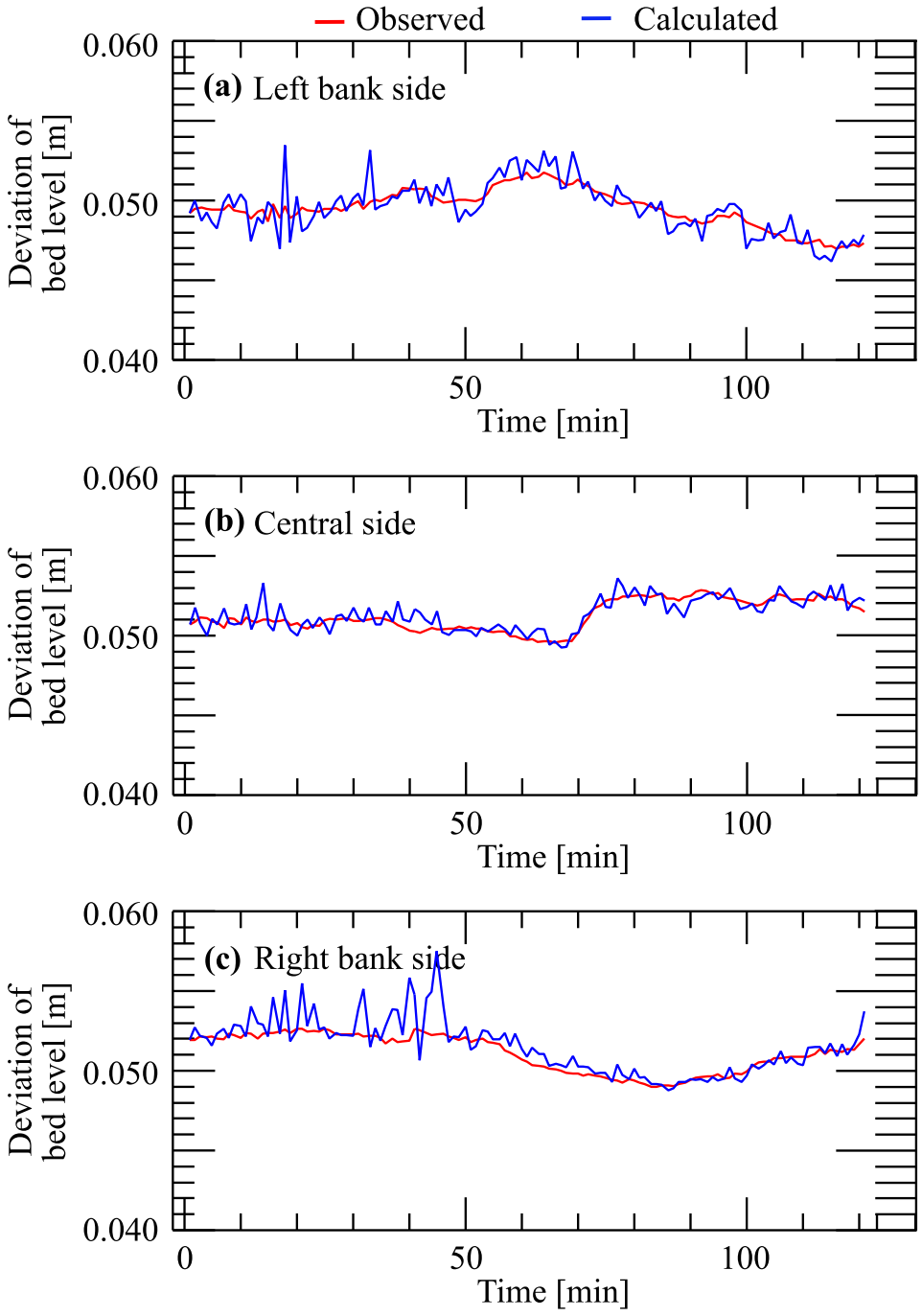

Figure 8. Bed-level time waveform: (a) Left bank side, (b) center, (c) right bank side.

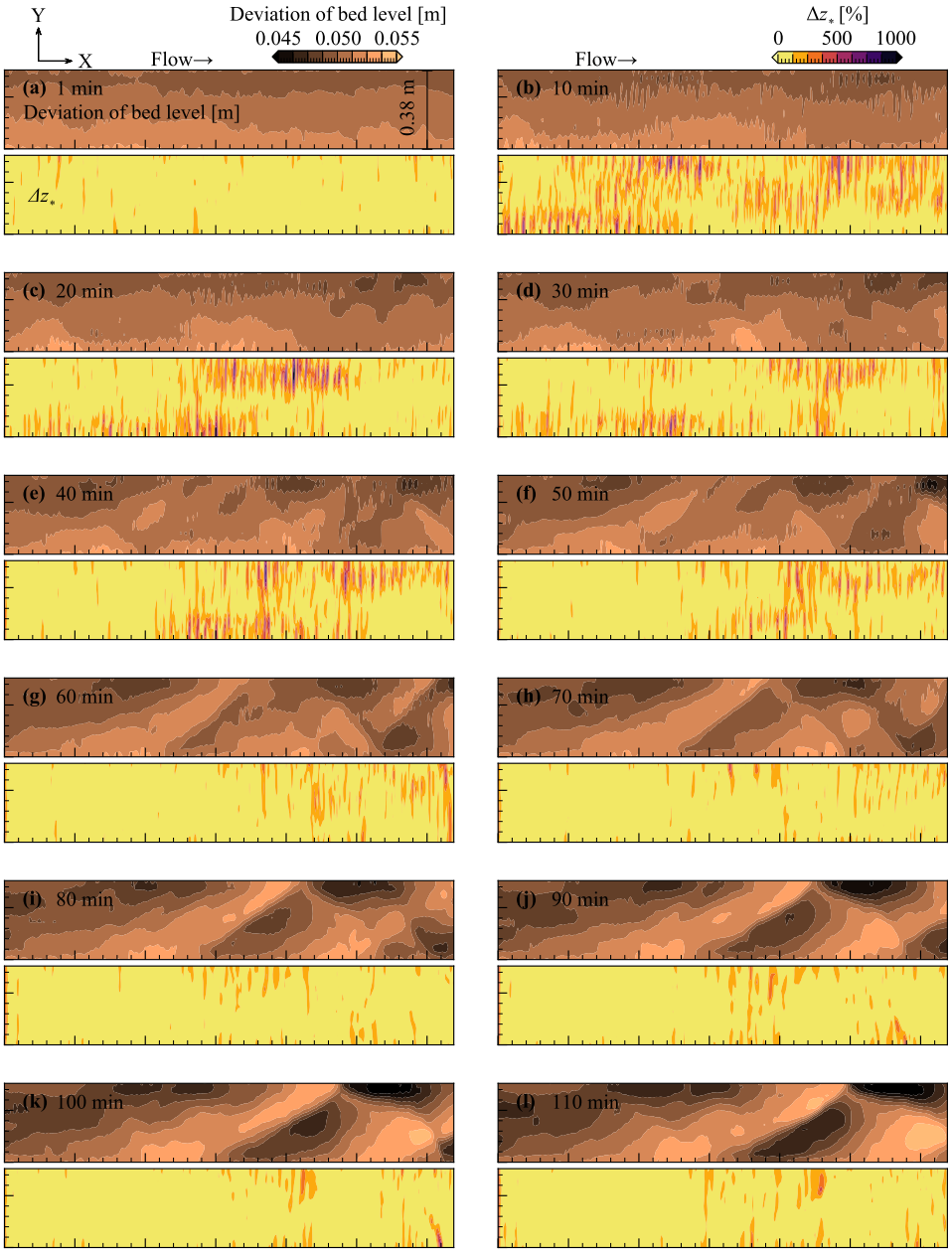

Figure 9. Temporal changes in the plan view for the observed bed topography and Δz_*.

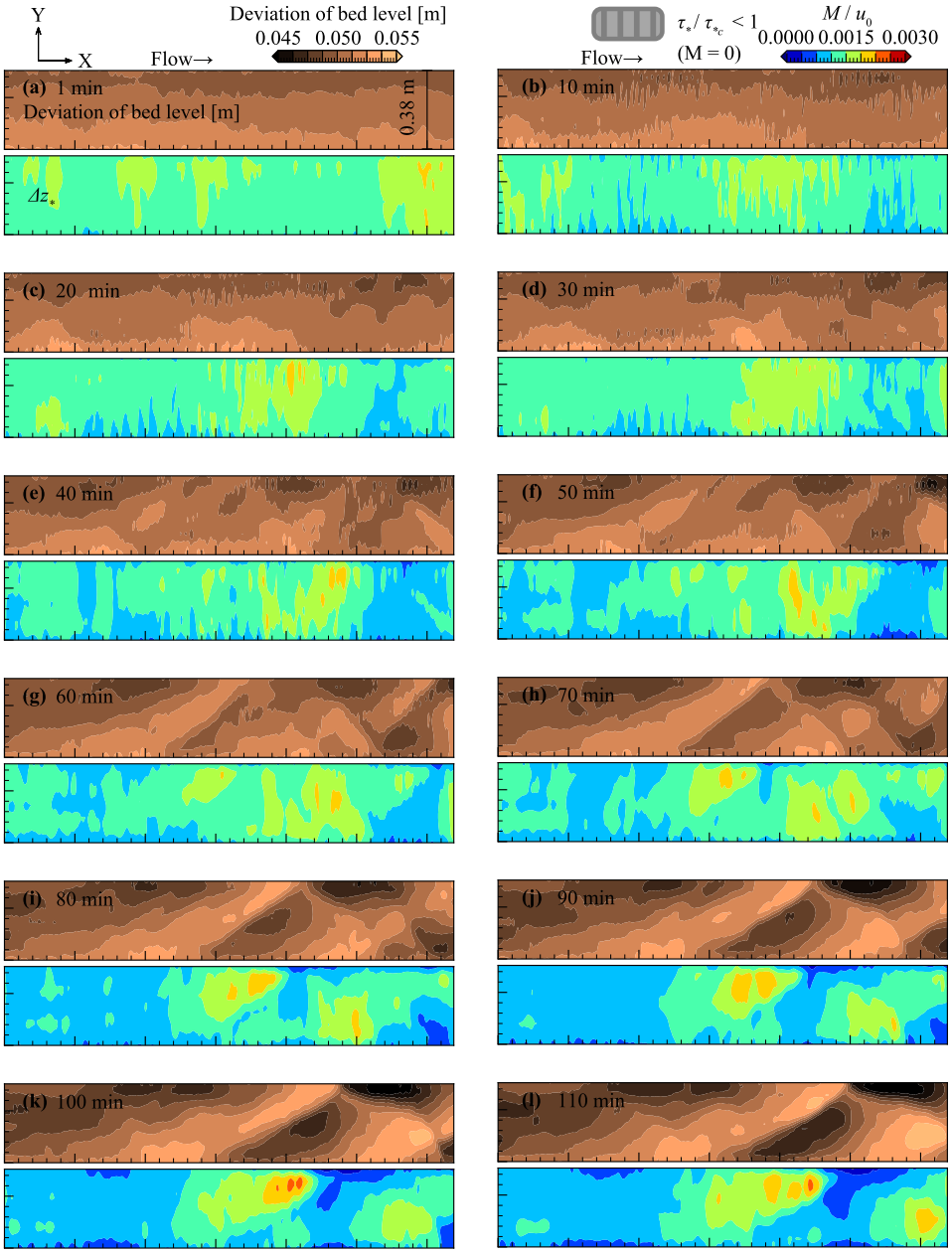

Figure 10. Temporal changes in the plan view for the observed bed topography and calculated migrating speed.

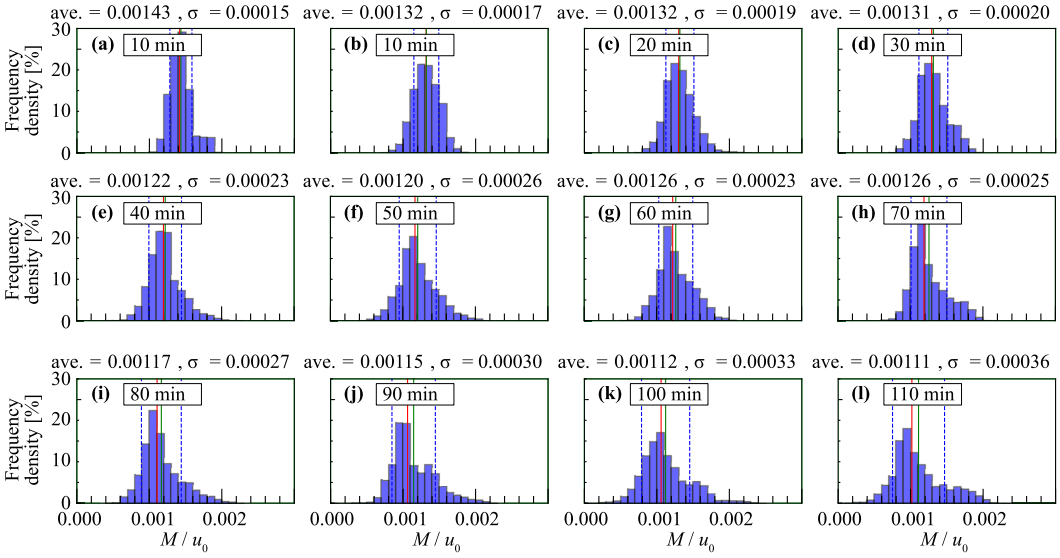

Figure 11. Histograms of migrating speed.

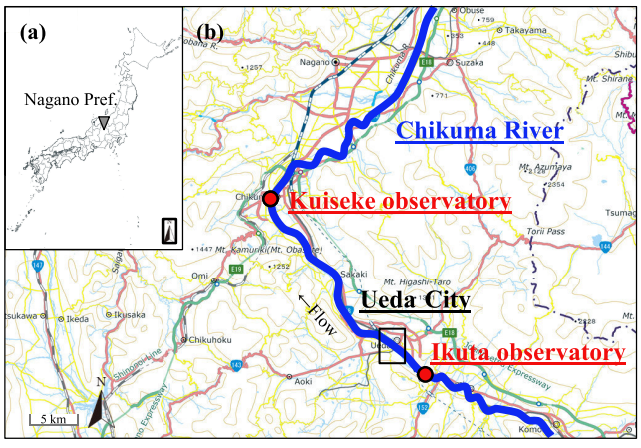

Figure 12. Overview of the study area: (a) geographic location, (b) map (GSI Maps (electronic land web) created by processing).

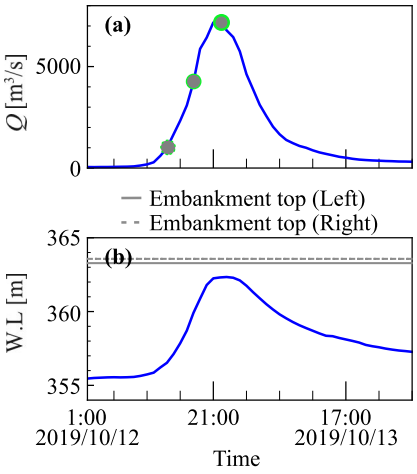

Figure 13. (a) Flow discharge hydrograph and (b) water level hydrograph.

Figure 14. Aerial photo of the target section: (a) Before the flood and (b) after the flood (「Part 2 Chikumagawa teibou chousa iinnkai shiryou」(Ministry of Land, Infrastructure, Transport and Tourism) (https://www.hrr.mlit.go.jp/river/chikumagawateibouchousa/chikuma-02.pdf) created by processing), Fig. 1 with water route added.

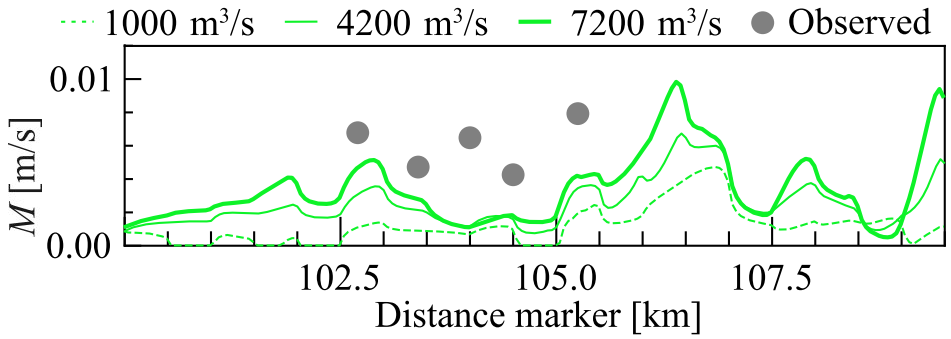

Figure 15. Calculated and measured values of migrating speed.

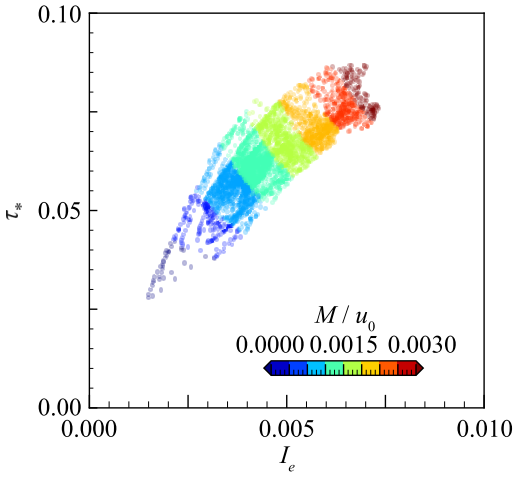

Figure 16. Relationship between energy slope, Shields number, and migrating speed.

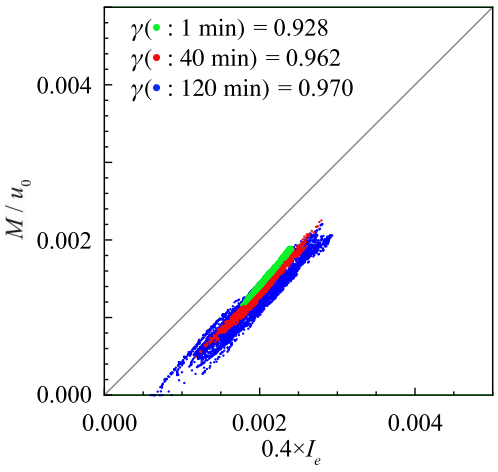

Figure 17. Relationship between migrating speed and energy slope.

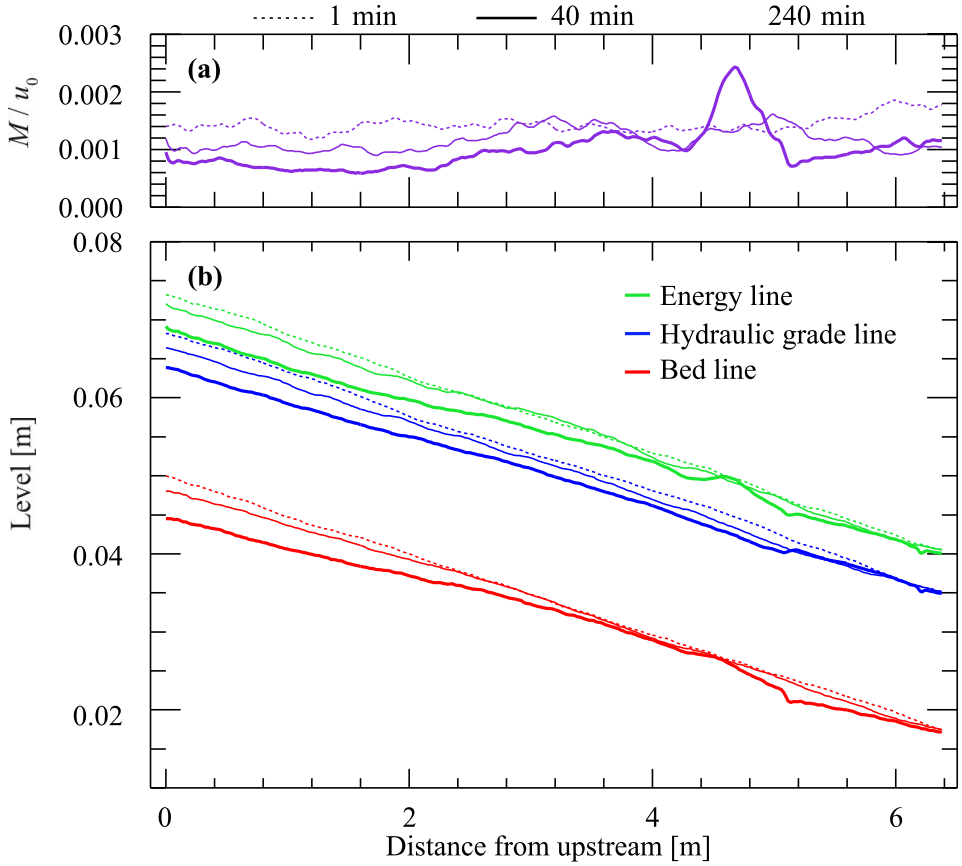

Figure 18. Longitudinal view of the (a) cross-sectional averaged migrating speed (b) and cross-sectional averaged bed level.

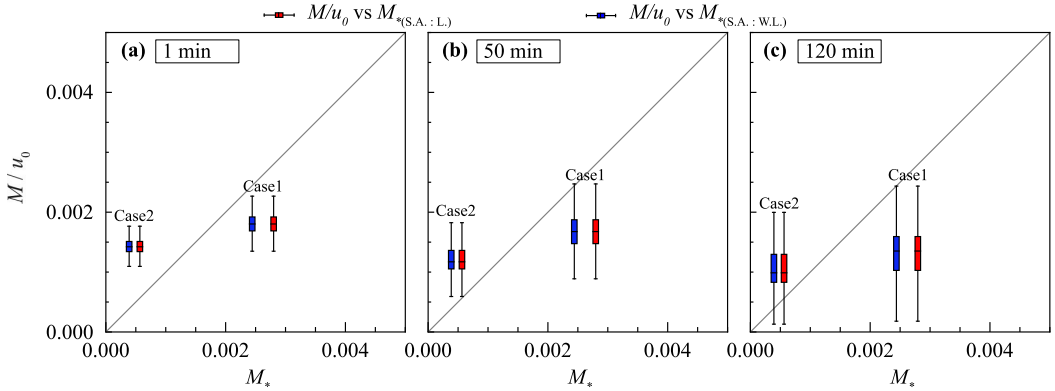

Figure 19. Relationship between migrating speed obtained by our method and migrating speed obtained by instability analysis.

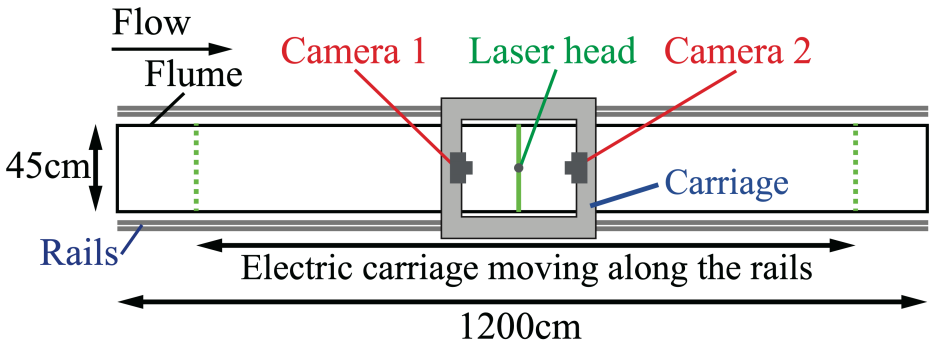

Figure A1. Plan view of the measuring device and flume.

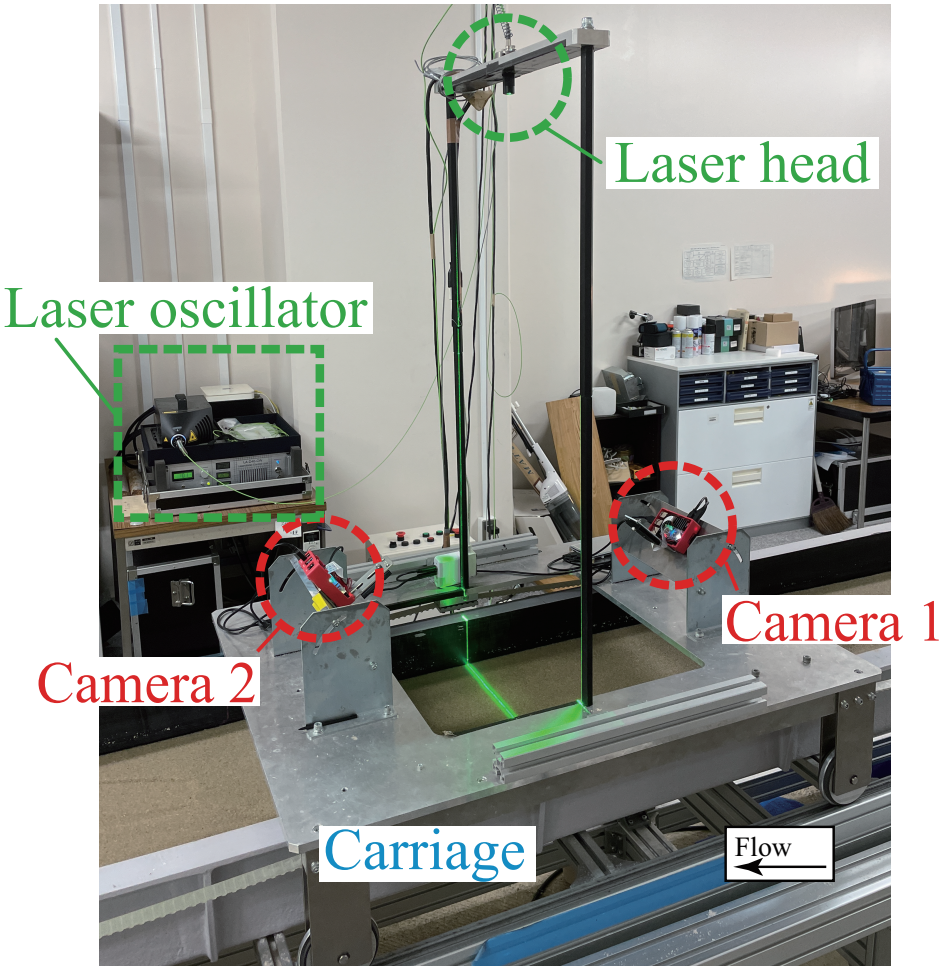

Figure A2. Equipmental layout of the measuring device.

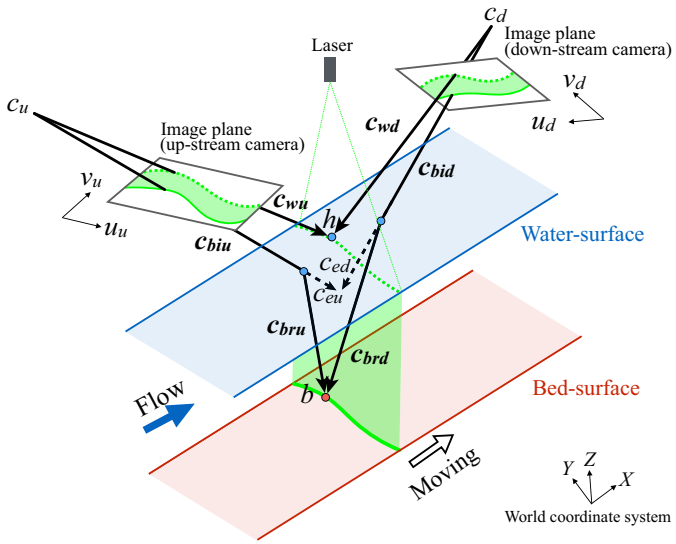

Figure A3. Outline of the geometric relations. C_u and C_d are the camera positions. h is calculated by observing the laser reflection on the water surface and is the intersection of the two observation vectors C_{wu} and C_{wd}. Reflection on the bed surface is observed at the position where it is refracted by the camera, $C_{biu} + C_{eu}(C_{bid} + C_{ed})$. By correcting the refracted reflection vector of the bed surface at the intersection point with the water surface, the observed vector of the bed surface becomes $C_{biu} + C_{bru}(C_{bid} + C_{brd})$.

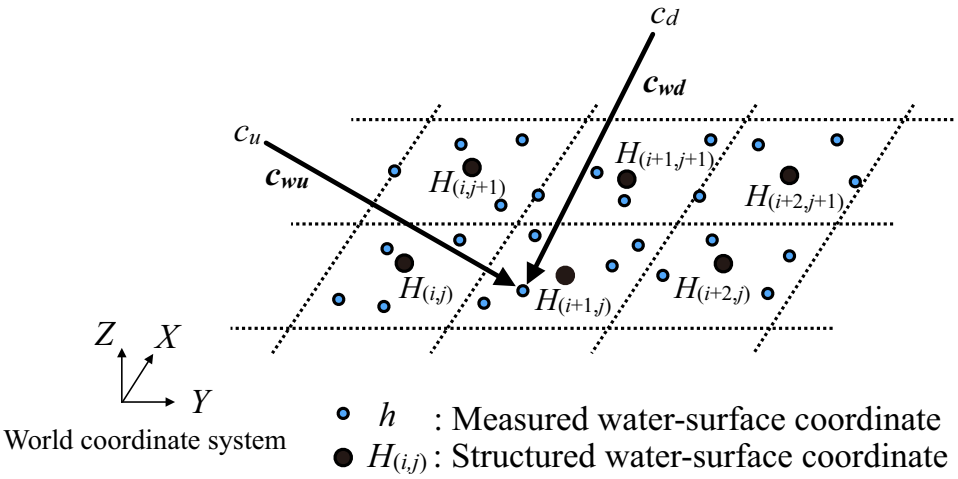

Figure A4. The structure-type function of the water level $H_{(i,j)}$, which is used for the refraction correction, is created from the calculated point cloud of h using the nearest point of the structure grid center coordinates.

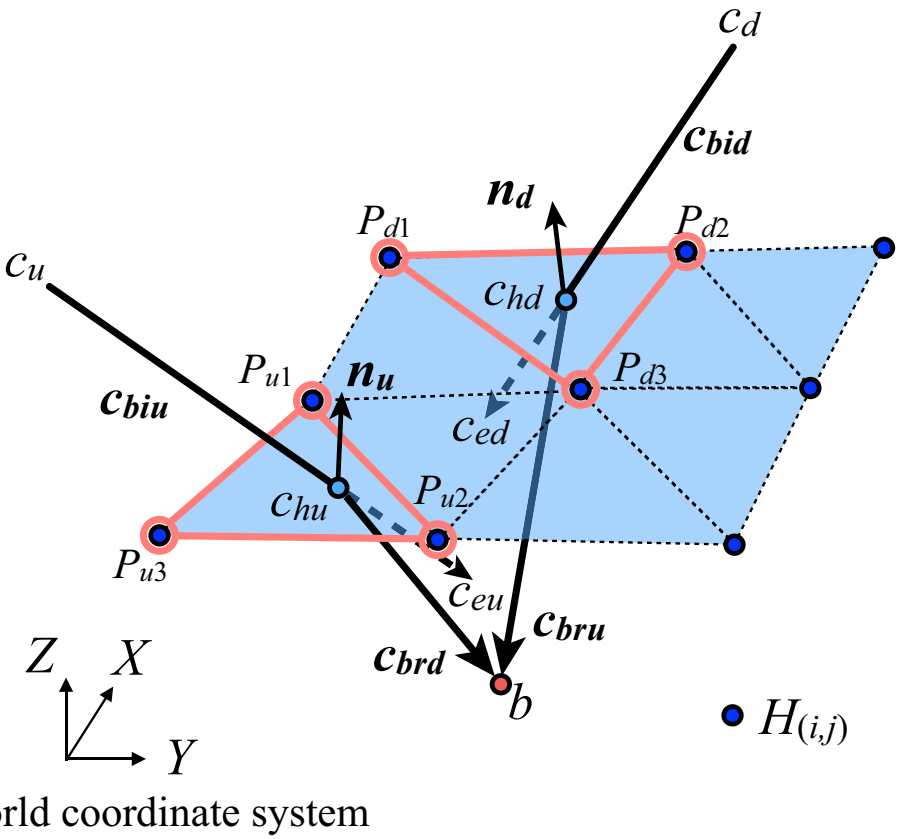

Figure A5. Schematic representation of the geometric relations in refraction correction. The refraction correction based on Snell's law requires water surface gradient $n_u(n_d)$ at $C_{hu}(C_{hd})$. The water levels P_{u1},P_{u2},P_{u3}(P_{d1},P_{d2},P_{d3}) at the three surrounding points are used to calculate $n_u(n_d)$.

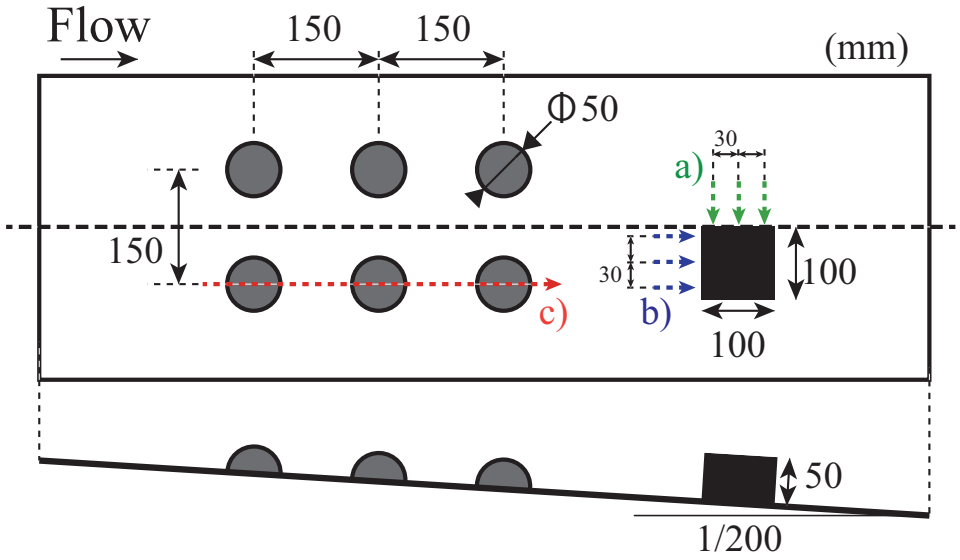

Figure A6. Arrangement of the objects of fixed-floor verification. The upper and lower panels show plan and cross-sectional views of the channel, respectively. The radius of the hemisphere is 25 mm, and the dimensions of the rectangle are 100×100×50 mm(width×length×height). The arrows in a) to c) indicate the measurement lines in the subsequent verification.

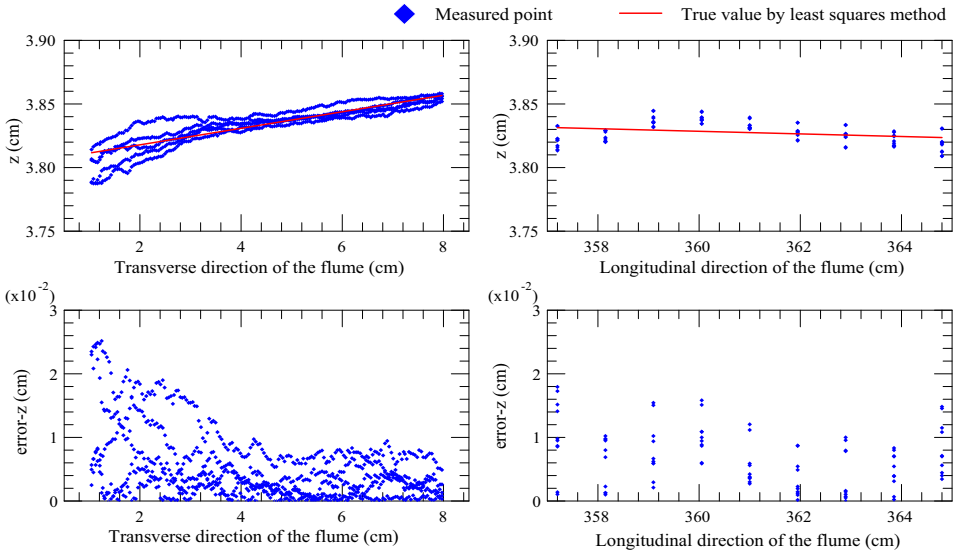

Figure A7. (Left) Upper figure shows the results of transverse measurements on the top surface of a rectangular area under dry conditions. Five measurements at 3-cm intervals in the longitudinal direction were superimposed by blue dots (15 sections in total). The red line is the estimated value obtained by the least-squares method and is regarded as the true value. The lower figure shows the z-error between the true and measured values. (Right) As in the left figure, the upper figure shows measurement results in the longitudinal direction. The results of five measurements at 3 cm in the transverse direction are superimposed.

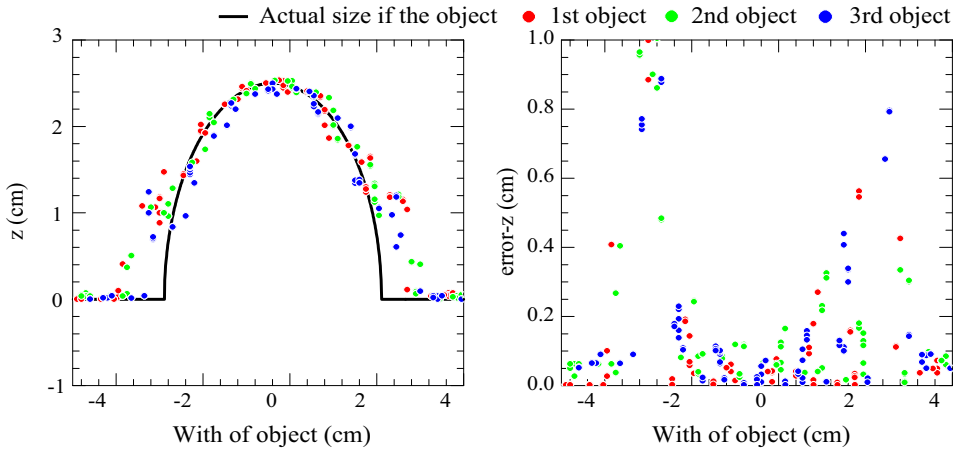

Figure A8. (Left) Results of five measurements in the longitudinal direction for three hemispheres on the right side under dry conditions are superimposed (15 sections in total). The measurement line was chosen to pass through the hemispherical center. The solid black line is the true value, which is a semicircle of radius 2.5 cm. (Right) The z-error between the true and measured values.

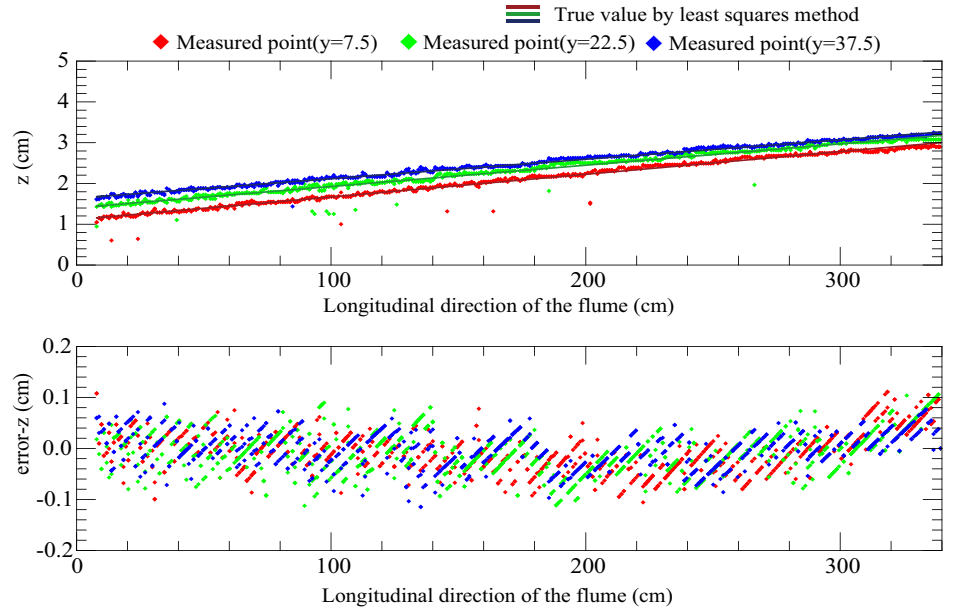

Figure A9. (Upper) Measurement results of the longitudinal section on the still water surface are shown for each measurement line, color-coded according to the distance from the starting point. The water depth increased longitudinally owing to the weir condition. The solid line of each color is the true value obtained using the least-squares method in each lateral direction. (Lower) The z-error between the true and measured values.

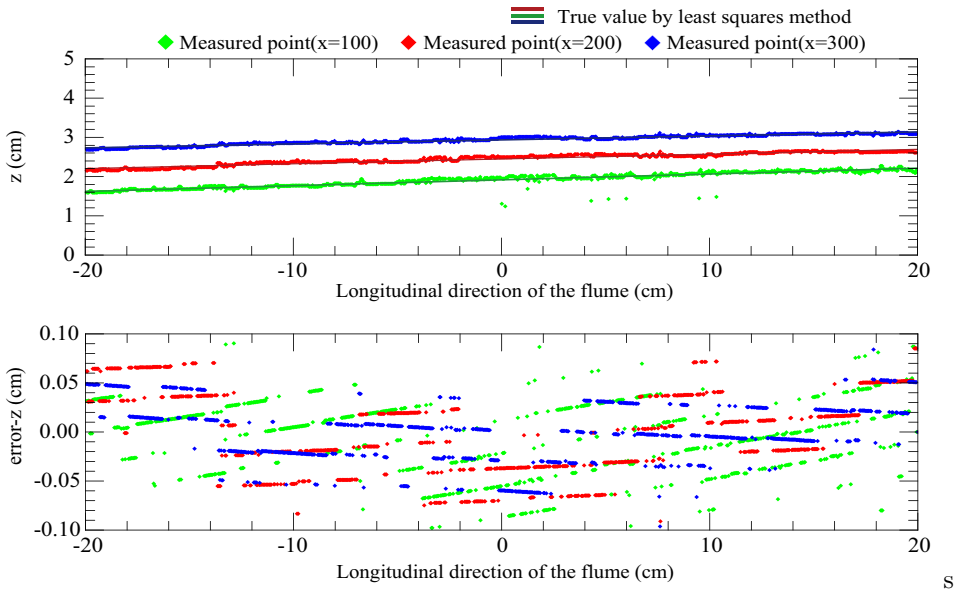

Figure A10. (Upper) Measurement results of the transverse section at the still water surface are shown by color-coding each measurement line according to the distance from the right bank. The solid line of each color is the true value obtained using the least-squares method for each lateral section. (Lower) The z-error between the true and measured values.

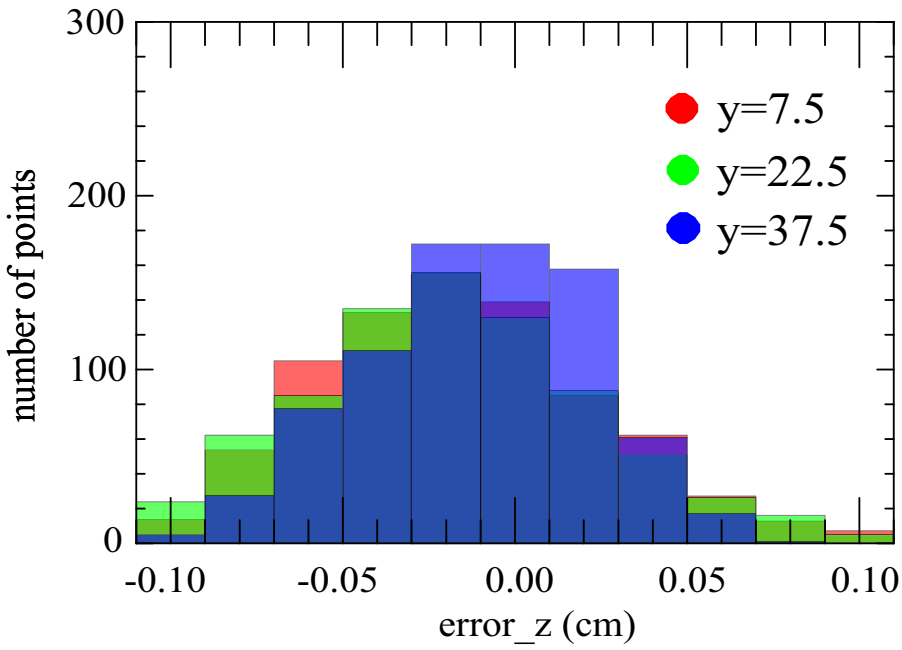

Figure A11. Histogram of the longitudinal z-error in still water surface measurements.

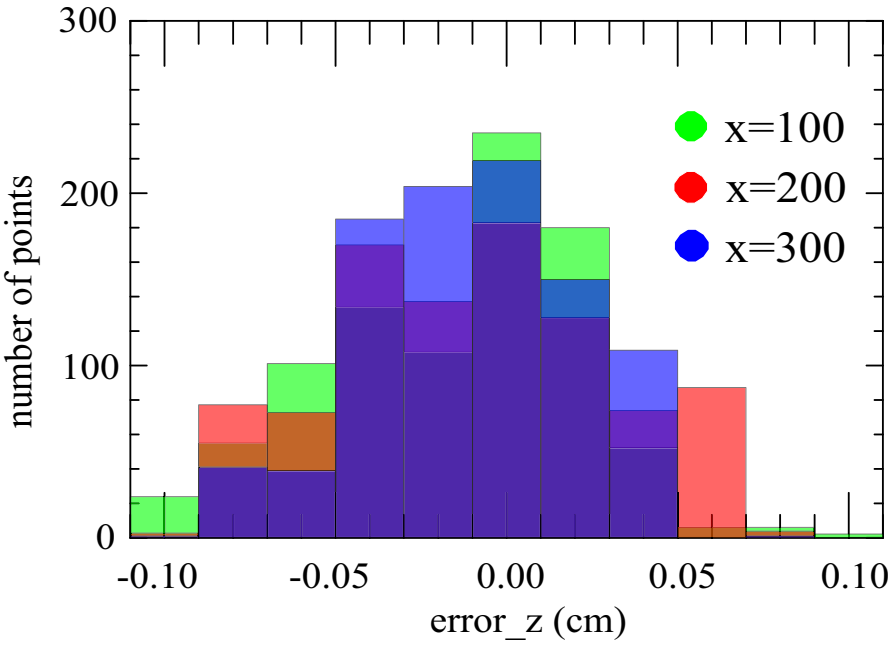

Figure A12. Histogram of the transverse z-error in still water surface measurements.

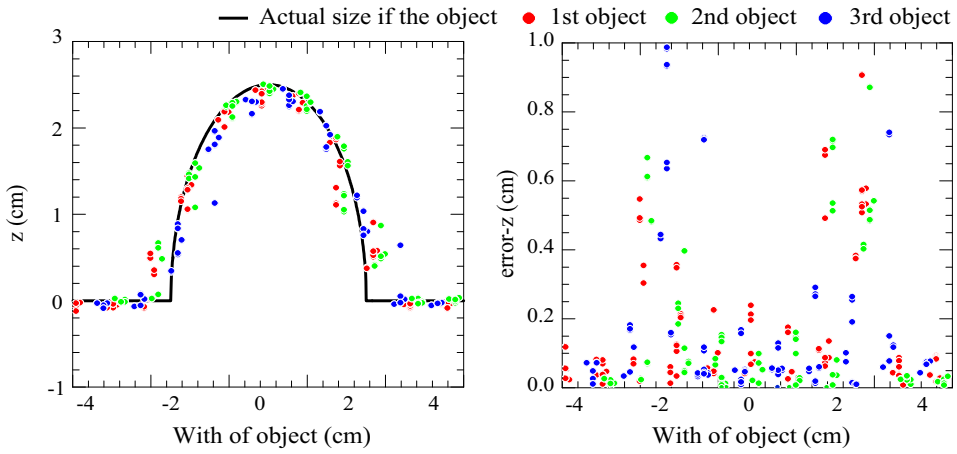

Figure A13. (Left) Results of five measurements in the longitudinal direction for the three hemispheres on the right side under still water conditions are superimposed (15 sections in total). The measurement line was chosen to pass through the hemispherical center. The solid black line is the true value, which is a semicircle of radius 2.5 cm. (Right) The z-error between the true and measured values.

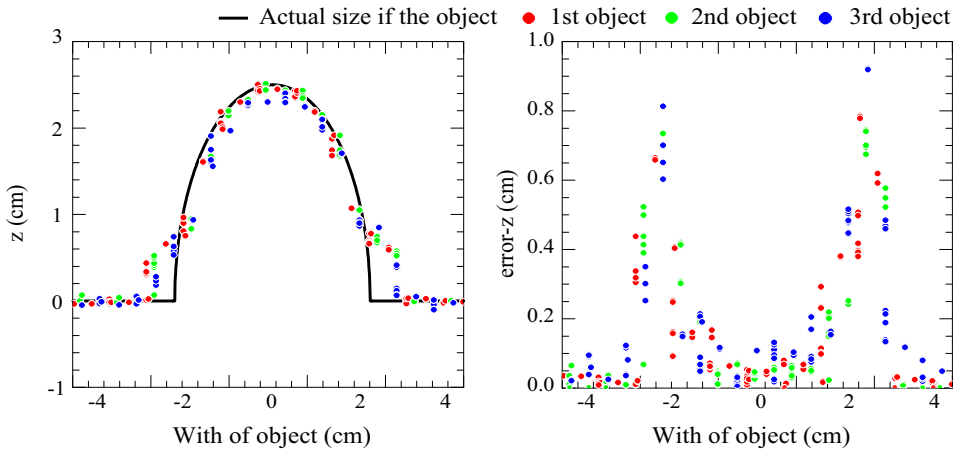

Figure A14. (Left) Results of five measurements in the longitudinal direction for the three hemispheres on the right side under flowing water conditions are superimposed (15 sections in total). The measurement line was chosen to pass through the hemispherical center. The solid black line is the true value, which is a semicircle of radius 2.5 cm. (Right) The z-error between the true and measured values.

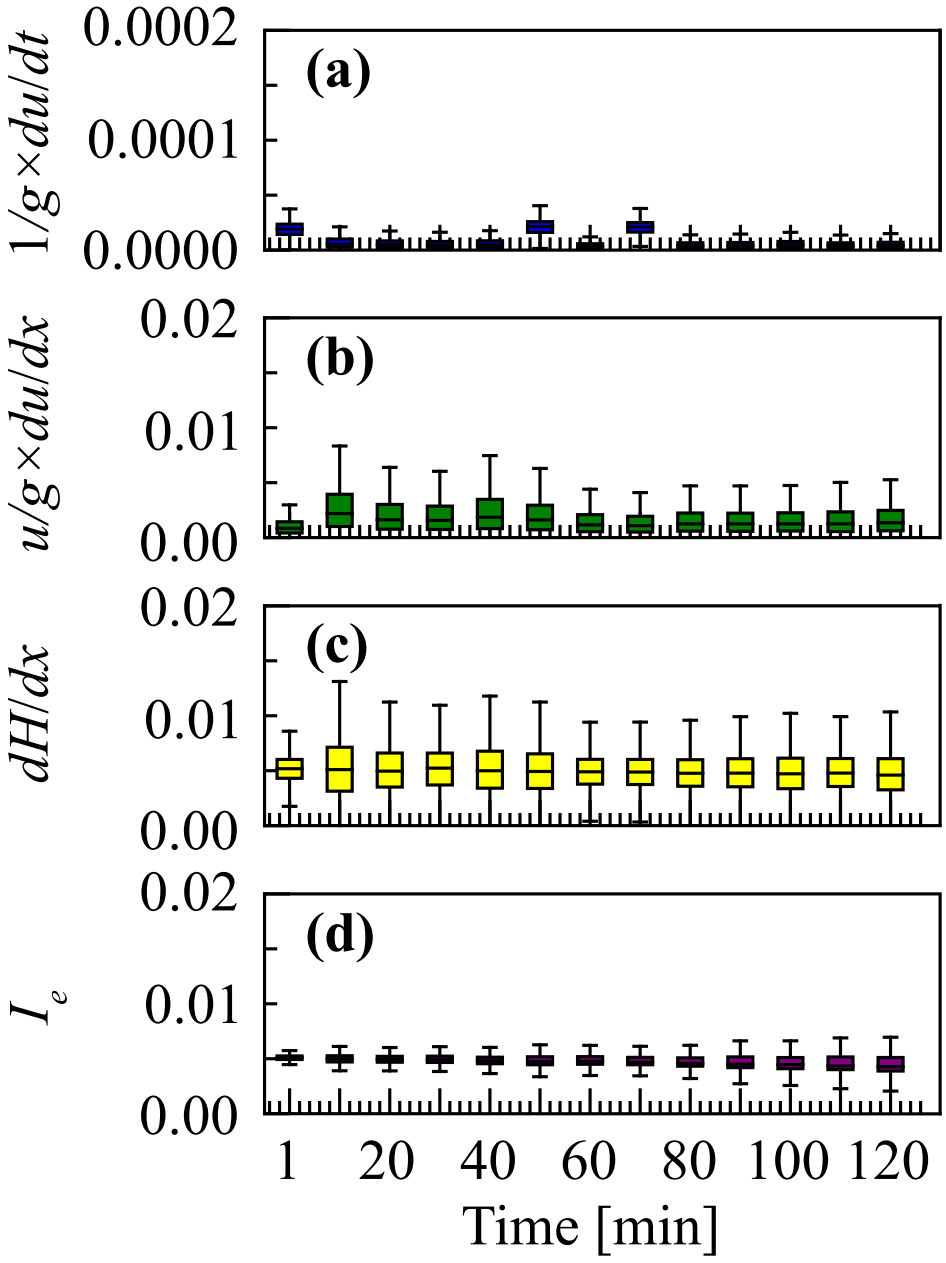

Figure B1. Temporal changes of the box plots for the (a) local term, (b) advection term, (c) pressure term, (d) and friction term.